

Physical constraints for respiration in microbial hotspots in soil and their importance for denitrification

Steffen Schlüter¹, Jan Zawallich², Hans-Jörg Vogel¹, Peter Dörsch³

¹ Department Soil System Sciences, Helmholtz-Centre for Environmental Research - UFZ,

5 Theodor-Lieser-Str. 4, 06120 Halle, Germany

² Institute of Mathematics, TU Clausthal, Erzstr. 1, Clausthal-Zellerfeld, Germany

³ Faculty of Environmental Sciences and Natural Resource Management, Norwegian University of Life Sciences, NMBU, Aas, Norway

correspondence to: Steffen Schlüter (steffen.schlueter@ufz.de)

10 **Abstract** Soil denitrification is the most important terrestrial process returning reactive nitrogen to the atmosphere, but remains poorly understood. In upland soils, denitrification occurs in hotspots of enhanced microbial activity, even under well-aerated conditions, and causes harmful emissions of nitric (NO) and nitrous oxide (N₂O). Timing and magnitude of such emissions are difficult to predict due to the delicate balance of oxygen (O₂) consumption and diffusion in soil.

15 To study how spatial distribution of hotspots affects O₂ exchange and denitrification, we embedded microbial hotspots composed of porous glass beads saturated with growing cultures of either *Agrobacterium tumefaciens* (a denitrifier lacking N₂O reductase) or *Paracoccus denitrificans* (a "complete" denitrifier) in different architectures (random vs. layered) in sterile sand that was adjusted to different water saturations (30%, 60%, 90%). Gas kinetics (O₂, CO₂,

20 NO, N₂O and N₂) were measured at high temporal resolution in batch mode. Air connectivity, air distance and air tortuosity were determined by X-ray tomography after the experiment. The hotspot architecture exerted strong control on microbial growth and timing of denitrification at low and intermediate saturations, because the separation distance between the microbial hotspots governed local oxygen supply. Electron flow diverted to denitrification in anoxic hotspot centers

25 was low (2-7%) but increased markedly (17-27%) at high water saturation. X-ray analysis revealed that the air phase around most of the hotspots remained connected to the headspace even at 90% saturation, suggesting that the threshold response of denitrification to soil moisture could be ascribed to increasing tortuosity of air-filled pores and the distance from the saturated hotspots to these air-filled pores. Our findings suggest that denitrification and its gaseous product
30 stoichiometry do not only depend on the amount of microbial hotspots in aerated soil, but also on their spatial distribution. We demonstrate that combining measurements of microbial activity with quantitative analysis of diffusion lengths using X-ray tomography provides unprecedented insights into physical constraints regulating soil microbial respiration in general and denitrification in particular. This paves the way to using observable soil structural attributes to
35 predict denitrification and to parameterize models. Further experiments with natural soil structure, carbon substrates and microbial communities are required to devise and parametrize denitrification models explicit for microbial hotspots.

1. Introduction

Soil carbon and nitrogen turnover is governed by soil heterogeneity at the microscale. Much of
40 the turnover is concentrated in microsites, providing favorable conditions (pO_2 , temperature, pH) and substrates (carbon, nutrients) for soil microbial activity. The partitioning of aerobic and anaerobic respiration in microsites is largely controlled by the water content in the soil matrix which defines the scale across which O_2 diffuses towards microsites of high O_2 -consuming activity. Aqueous diffusion lengths range from distances across thin water films in well-aerated
45 soils, to individual soil aggregates of different radii at field capacity, up to the distance to the soil surface when the soil is saturated (Smith et al., 2003;Elberling et al., 2011;Ball, 2013;Parkin, 1987). Aerobic respiration is less affected by soil moisture than anaerobic respiration and

typically peaks around water saturations of 20-60% (Schaufler et al., 2010;Ruser et al., 2006;Moyano et al., 2012). Bulk soil respiration starts to decline at higher saturations due to the
50 development of anoxic microsites with lower redox potential, supporting carbon mineralization at typically only a tenth of the rates observed under oxic conditions (Keiluweit et al., 2017). Denitrification, i.e. the dissimilatory respiration of N oxyanions instead of oxygen, is commonly observed at water saturations above 60-70% and peaks beyond 90% (Ruser et al., 2006;Linn and Doran, 1984). The occurrence of anaerobic microsites is governed by the balance between
55 saturation-dependent diffusion and microbial consumption of O₂, which in turn depends on the quantity, quality and distribution of soil organic matter in the soil matrix and environmental factors like temperature and pH, which control microbial activity (Tecon and Or, 2017;Nunan, 2017;Smith et al., 2003). In fact, water films around decaying plant material may suffice to induce anaerobic respiration, if microbial respiration exceeds O₂ diffusion through that minute
60 barrier (Parkin, 1987;Kravchenko et al., 2017).

The interplay between physical constraints and biological activity in soil controls microbial respiration at microscopic scales and complicates the prediction of denitrification and N-gas fluxes at larger scales. For instance, nitrous oxide (N₂O) emissions are notoriously variable in space, which has been attributed to heterogeneous distribution of anoxic microsites in the soil
65 (Mathieu et al., 2006;Röver et al., 1999;Parkin, 1987;Parry et al., 1999). Together with the often observed high temporal variability of microbial respiration and its fluctuations under transient conditions, this has led to the notion of “hotspots” and “hot moments” for microbial activity and emissions (Groffman et al., 2009;Kuziyakov and Blagodatskaya, 2015). “Hotspots” of denitrification have traditionally been linked to diffusion constraints in soil aggregates (Smith,
70 1980;Arah and Vinten, 1995). Cell numbers and O₂ concentration have been shown to decline exponentially towards aggregate centers (Sexstone et al., 1985;Horn et al., 1994;Zausig et al.,

1993;Højberg et al., 1994) and the critical aggregate radius for the development of anoxic centers and is variable but typically >1 mm (Sierra and Renault, 1996;Højberg et al., 1994;Schlüter et al., 2018), However, anoxic microsites have also been reported for smaller aggregates (equivalent
75 diameter of 0.03-0.13 mm) in well-aerated, repacked soils (Keiluweit et al., 2018).

An important, but often neglected aspect of physical diffusion constraints on microbial respiration is the spatial distribution of microbial hotspots within the soil matrix. Incubation experiments were either designed to control the aggregate size in repacked soil (Mangalassery et al., 2013;Miller et al., 2009) or the volume fraction of sieved soil mixed evenly into sterile quartz
80 sand (Keiluweit et al., 2018). Some incubation studies were carried out with undisturbed soil and investigated diffusion constraints within the pore network (Rabot et al., 2015). However, these studies did not address the spatial distribution of hotspots nor the diffusion lengths towards air-filled pores. The vast majority of incubations studies merely reports bulk soil properties like carbon and nitrogen content, bulk density and water saturation. Notable exceptions are
85 Kravchenko et al. (2017) who controlled the position of microbial hotspots by placing decaying plant leaf material into repacked soils with different aggregate sizes and water saturations and Ebrahimi and Or (2018), who placed several layers of remolded aggregates as artificial hotspots into a sand matrix and controlled the volume fraction of anaerobic and aerobic respiration by adjusting the water table in the sand column. Such systematic studies with simplified soil
90 aggregate analogues, yet fully accounting for transport processes from and towards hotspots, including interactions between hotspots, are needed to improve our understanding about how physical constraints on microbial respiration control the anaerobic soil volume and hence denitrification activity.

The objective of the present study was to study the interplay between microbial activity and physical diffusion in controlling aerobic and anaerobic respiration for different spatial distributions of hotspots. We embedded uniform artificial hotspots saturated with oxically growing denitrifier pure cultures (Schlüter et al., 2018) in sterile sand in two different architectures: either densely packed in two layers with minimal distance between hotspots within a layer or distributed randomly with maximum spacing between individual hotspots (Figure 1a-
b). We presumed that the competition for oxygen would depend on this separation distance between the hotspots, which in turn would control microbial cell growth and O₂ consumption and thus affect the timing and velocity of the aerobe-anaerobe transition in respiration with consequences for the onset of denitrification and its gaseous product stoichiometry. Further, by placing hotspots with complete (*P. denitrificans*) and truncated (*A. tumefaciens*) denitrifiers in distinct horizontal layers, we expected to see interactions between hotspots acting as mere N₂O sources and hotspots potentially being N₂O sinks (by reducing N₂O to N₂). To create contrasting velocities of oxygen transfer between headspace and hotspots, we incubated the different hotspot architectures at three water saturations thereby addressing the question how overall oxygen supply (regulated by saturation) and local oxygen availability (regulated by hotspot distribution) interact in regulating denitrification activity. The overall goal of our reductionist approach with artificial hotspots, pure bacterial strains and a closed incubation system was to reduce the inherent complexity of soil in order to (i) identify processes that governed denitrification at the pore scale and (ii) create an experimental dataset for validation of pore-scale denitrification models.

For this, we monitored O₂, CO₂, NO, N₂O and N₂ at high temporal resolution and determined the morphology of the air-filled pore space in terms of air connectivity, air tortuosity and air distance by X-ray computed tomography after the experiment.

2. Material and methods

2.1. Microbial hotspots

Two denitrifier strains were used in this study: *Paracoccus denitrificans* expresses all
120 denitrification enzymes necessary to reduce NO_3^- to N_2 , whereas *Agrobacterium tumefaciens*
lacks the gene *nosZ* encoding nitrous oxide reductase (N_2OR), which makes N_2O the final
denitrification product. Moreover, the two strains differ in their regulatory phenotypes with
respect to inducing denitrification in response to oxygen depletion, which leads to characteristic
patterns of product accumulation (Bergaust et al., 2011). *P. denitrificans* induces NO and N_2O
125 reductase early during O_2 depletion (Bergaust et al., 2010), thus releasing little N_2O . By contrast,
A. tumefaciens is known to be less stringent in controlling intermediates, which may result in the
release of large amounts of NO , up to cell-toxic, milli-molar concentrations (Bergaust et al.,
2008). Both strains were grown oxically in Sistrom's medium (Sistrom, 1960) as described in a
previous study (Schlüter et al., 2018), but at double strength to provide enough substrate for
130 depleting O_2 during aerobic growth once transferred to the porous glass beads. The medium was
amended with 10 mM NH_4NO_3 and 5 mM KNO_3 for anaerobic growth. To produce microbial
hotspots, porous borosilicate glass beads (VitraPOR P100, ROBU Glasfilter Geräte GmbH) with
a diameter of 7 mm, a porosity of 32% and a medium pore diameter of 60 μm were saturated with
freshly inoculated growth medium ($\approx 10^8$ cells ml^{-1}) by submersion into one of the two cultures. In
135 the following, the inoculated porous glass beads are referred to as *At-* (*A. tumefaciens*) and *Pd-*
(*P. denitrificans*) hotspots. Detailed information about the culture conditions and the inoculation
procedure can be found in Schlüter et al. (2018).

2.2. Repacked sand

Fifty *At* and *Pd* hotspots each were placed into 120 ml of washed, sterile quartz sand (0.2-0.5 mm grain size) yielding a volume fraction of 14% (20 ml; Fig. S1a). The sand was packed into 240 ml glass jars (Ball Corporation, Bloomfield, CA) in portions of 10 ml layers and adjusted to target saturation by adding sterile water with a spray can. The packing procedure resulted in some minor changes in porosity between layers and some larger gaps around the hotspots (Fig. S3) which affected air distribution in the sand (Fig. S2a). Three saturations were used, corresponding to water-filled pore spaces (WFPS) of 30, 60 and 90%. The fully saturated hotspots were placed into the sand at three different architectures (Fig. 1). For the “random” distribution, the hotspots were placed in five equidistant (~9.8 mm, center to center) horizontal layers with a random distribution of ten *At* and ten *Pd* hotspots per layer. The average spacing between neighboring hotspots (surface to surface) was approx. 6mm in this architecture, which was the maximum possible spacing for this amount of hotspot volume (Fig. 1b). For the “layered *At/Pd*” and “layered *Pd/At*” distributions, all fifty hotspots of each strain were placed into one of two horizontal layers spaced 21 mm from each other (center to center) at an average headspace distance of 18.2 and 39.2 mm, respectively, where the order represents *top/bottom*. The average spacing between neighboring hotspots (surface to surface) was approx. 1 mm in these densely packed layers (Fig. 1c). Care was taken to keep the hotspots cool (on crushed ice) during the packing procedure. The pore size distribution of the porous hotspots and the sand in the bulk soil and in hotspot vicinity are reported in Figure S3.

2.3. Incubation

To establish aerobic and anaerobic growth patterns and denitrification kinetics for both bacterial strains when growing inside the porous glass beads, a pre-experiment was conducted without

sand. Fifty *Pd* or *At* hotspots were placed in septum-sealed 120 ml serum bottles (Fig. S1b) and incubated at 15°C under either oxic (He/O₂ 80/20%) or anoxic (He 100%) conditions in two replicates per treatment. Headspace concentrations of O₂, CO₂, NO, N₂O and N₂ were measured every 4 h by piercing the septum with a hypodermic needle mounted to the robotic arm of an autosampler (GC-PAL, CTC Analytics, Switzerland). The autosampler was connected to a gas chromatograph (Agilent Model 7890A, Santa Clara, CA, USA) and a NO analyzer (Teledyne 200, San Diego, CA, USA) via a peristaltic pump. Detailed information about the robotized incubation system and the experimental setup can be retrieved elsewhere (Molstad et al., 2007; Schlüter et al., 2018).

170 In the main experiment, freshly inoculated glass beads were packed into incubation vessels as described above, three replicates for each of the nine combinations of saturation and hotspot distribution. Jars with 30% and 60% WFPS were flushed with He/O₂ for 40 min, using ten cycles of vacuum (3 min) and purging (1 min). Jars with 90% WFPS were flushed using 180 cycles of mild vacuum (~ 600 mbar) and O₂/He purging to avoid structural changes of the packed columns due to bubbling of trapped gas. The jars were then placed into a water bath kept at 15°C and after temperature equilibration O₂/He overpressure was released. Gas concentrations in the headspace were analyzed as described above. Gas production and consumption kinetics were used to calculate the fraction of electrons diverted to O₂ or N oxyanions and thus to estimate the contribution of denitrification to total respiration (e_{denit}^-/e_{total}^-) (Schlüter et al., 2018; Bergaust et al., 2011). The NO/(NO+ N₂O + N₂) and N₂O/(NO+ N₂O + N₂) product ratios were estimated from the cumulative release of gaseous denitrification products (NO, N₂O, N₂), after subtracting precursors from products (NO from N₂O + N₂ and NO + N₂O from N₂). The rationale behind the latter was to mimic an open system, in which N-gases released to the atmosphere are not available any longer as electron acceptors for denitrification. This approach cannot make up for

185 the general shortcoming of closed systems that accumulate gaseous and dissolved intermediates to high concentrations, but N₂O concentrations in soil air reaching >100 ppm are reported occasionally (Risk et al., 2014; Russenes et al., 2019). Details about the calculation of denitrification product ratios can be found in the Supporting Information (SI 1.2).

2.4. X-ray tomography and image analysis

190 After the incubation experiment, the glass jars were scanned with X-ray micro-tomography (X-tek XCT 225, Nikon Metrology) with a beam energy of 145 kV, a beam current of 280 μA, an exposure time of 708 ms per frame, a 0.5 mm copper filter for reducing beam hardening artefacts and a total of 3000 projection for a full scan. Individual hotspots were also scanned (100 kV, 90μA, 1000ms per frame, no filter) to analyze the internal pore morphology. The 2D projections
195 were reconstructed into a 3D image with a resolution of 35 μm using a filtered-back projection algorithm in the X-tek CT Pro 3D software. Image processing from raw gray-scale data (**Fig. 1a**) to segmented data including sand grains, air and water (**Fig. 1b-c**) was carried out according to well-established protocols for multi-phase segmentation (Schlüter et al., 2014). The porous glass beads were assigned to *At* or *Pd* hotspots according to the orientation of the flat end in the
200 random architecture or by the vertical position in the layered architecture (**Fig. 1b-c**). The segmented images were analyzed with respect to three different spatial attributes of the air-filled pore spaces deemed important for oxygen supply. 1. Air connectivity by distinguishing isolated air-filled pores and air-filled pores with a continuous path to the headspace (yellow and red in **Fig. 1d**). Air connectivity is then defined as the ratio of connected air-filled pore space and total
205 air-filled pore space 2. Air tortuosity as derived from the geodesic length of connected air-filled pores. The geodesic length is the distance of any connected air voxel to the headspace along curved paths around obstacles like solid particles and water-blocked pores (**Fig. 1e**). Air

tortuosity is the ratio between geodesic and vertical Euclidean distance to the headspace averaged over all connected, air-filled voxels. It is a proxy for the diffusive transport of gaseous oxygen in air-filled pores 3. Air distances of water-filled pores as defined by the average geodesic distance from any water voxel to the closest air-filled pore with headspace connection (white in **Fig. 1f**). Air distance is a proxy for the slow diffusive transport of dissolved oxygen. All image processing steps were carried out with Fiji/ImageJ (Schindelin et al., 2012) and associated plugins (Legland et al., 2016; Doube et al., 2010) or with VG Studio Max 2.1 (Volume Graphics). Each image processing and analysis step is explained in detail in the supporting information (**SI 1.3**).

[Figure 1]

3. Results

3.1. Aerobic respiration and denitrification in unconstrained hotspots without sand

At grew faster than *Pd* at 15°C in the experiment with loosely placed porous glass beads as indicated by faster O₂ consumption and CO₂ accumulation in the oxic treatment (**Figure 2a,b**). Also under fully anoxic conditions, *At* accumulated CO₂ faster than *Pd* (Figure 2b). N-gas kinetics clearly reflected the disparate regulatory phenotypes of the two bacterial denitrifiers. Anoxic *At* instantly accumulated large amounts of NO (**Figure 2c**) which persisted until all NO₃⁻ was reduced to N₂O (as judged from the stable plateau in N₂O, **Figure 2d**). Due to slower growth and O₂ consumption, *Pd* induced denitrification much later than *At*, but accumulated less intermediates (NO, N₂O) than *At*. Oxically incubated *Pd* accumulated no detectable NO, indicating efficient regulation of denitrification when switched slowly to anaerobic conditions in hotspots. Also, NO may have been reduced to N₂O when diffusing from the anoxic center to the

230 boundary of the hotspots. In the initially oxic treatments, denitrification contributed 7% to the total electron flow in *At* hotspots and 13% in *Pd* hotspots measured over the entire period, reflecting the fact that (i) *Pd* has one more reduction step in the denitrification sequence and that (ii) *At* used less nitrate for anaerobic respiration in anoxic hotspots centers and more oxygen for aerobic respiration in oxic hotspots margins than *Pd*.

235 [Figure 2]

3.2. Effects of hotspot distribution in sand

The distribution of microbial hotspots within the sand strongly impacted bulk respiration. This is evident for treatments with medium saturation (60% WFPS) for the first 210 h of incubation (**Figure 3**) and with other saturations for the entire incubation period (300 h; **Figures S4-6**). The random distribution of hotspots allowed for much faster aerobic growth than the layered architectures, leading to complete consumption of O₂ from the jars within 70 h (**Figure 3a**). Given the slow growth of *Pd* (**Figure 2a**), initial O₂ consumption was dominated by the activity of *At* hotspots turning them partly anoxic. Hence, the pronounced NO peak in the random treatment, coinciding with complete O₂ exhaustion from the headspace (**Figure 3c**), was due to *At* denitrification, similar to what was seen in the unconstrained *At* hotspots under anoxic conditions (**Figure 2c**). N₂O production was observed long before O₂ was depleted from the headspace (**Figure 3d**) and is attributed entirely to *At* denitrification. *Pd* denitrification did not start before all O₂ was depleted and manifested itself in a transient increase in N₂O production at ~70 h together with an exponential increase in N₂ production (**Figure 3e**) which was also observed with unconstrained *Pd* hotspots (**Figure 2e**). Note that the apparent net consumption of CO₂ (**Figure 3b**) upon O₂ depletion was due to internal alkalization driven by accelerating denitrification, once all hotspots turned anoxic.

[Figure 3]

In the layered architectures, O₂ consumption was slower and complete anoxia was not reached
255 before 120 h into the incubation. In contrast to the random architecture, less O₂ was available for
each individual hotspot in the densely packed hotspot layers, allowing for less aerobic growth per
unit time. As a consequence, there was more time for fully denitrifying *At* hotspots to interact
with *Pd* hotspots which induced denitrification gradually between 80 and 120 h. Indeed, less N₂O
accumulated in the headspace than in the random treatment (**Figure 3d, S6d**) and the onset of N₂
260 accumulation appeared long before complete O₂ depletion in the headspace (**Figure 3a,e**). In
other words, *Pd* hotspots consumed N₂O produced in *At* hotspots. Upon O₂ depletion in the
headspace, a burst of NO production occurred (**Figure 3c**) as seen previously with *At* hotspots
(**Figure 2c**). However, since *Pd* denitrification was now fully developed, the NO peak was much
more short-lived than with the random distribution, because *Pd* hotspots reduced NO produced by
265 *At* hotspots all the way to N₂.

The effect of vertical order in the layered hotspot architecture was small, but consistent among all
denitrification products. The distribution with *Pd* hotspots on top (layered *Pd/At*) consumed the
NO and N₂O produced in *At* hotspots much quicker than the *At/Pd* architecture (**Figure 3c-d**) and
accumulated N₂ faster after complete O₂ depletion (**Figure 3e**). Both observations highlight the
270 effect of shorter diffusion distances between the headspace and the *Pd* hotspot layer in the layered
Pd/At architecture.

3.3. Effects of matrix saturation

Differences in water saturation resulted in different absolute amounts of oxygen initially present
in the jars (**Figure 4a**) but did not affect the O₂ concentration in the sand matrix. Oxygen was

275 depleted slightly faster at 60% than at 90% saturation even though there was absolutely more O₂ initially present at 60% WFPS. This illustrates the paramount role of oxic growth for the oxic-anoxic transition in the hotspots: the more O₂ available initially, the stronger the aerobic growth and the faster the oxic-anoxic transition.

Increasing saturation from 60 to 90% in the randomly distributed hotspots had a strong effect on
280 the timing and accumulation of denitrification products. The expected NO burst upon O₂ depletion was damped by two orders of magnitude (**Figure 4c**), because the oxic-anoxic transition proceeded more smoothly in the 90% treatment and NO was reduced further to N₂O before it could escape to the headspace. On the other hand, N₂O and N₂ production commenced earlier in the 90% than in the 60% treatment (**Figure 4d-e**), indicating that O₂ availability was *a*
285 *priori* smaller irrespective of metabolic activity (which was larger in the 60% treatment). The switch from net N₂O production to net N₂O consumption indicates the moment when microbial activity in *Pd* hotspots caught up with *At* hotspots.

[Figure 4]

Surprisingly, O₂ consumption in the 30% treatments was slow despite having the largest amount
290 of O₂ in the jar. This was caused by unintended substrate limitation. Due to overlapping pore size distribution between porous hotspots and sand (**Fig. S3c**), medium was sucked by capillary force from the hotspot into the surrounding sand, as could be seen in a parallel experiment with brilliant blue dye (**Fig. S7**). This separated bacterial cells, which were likely immobilized in the pore space of the hotspots, temporarily from a considerable fraction of the carbon and NO₃⁻ supplied
295 with the medium, before the dissolved substrate would diffuse back into the hotspots due to the evolving gradient induced by consumption in the hotspots. Decreasing the saturation from 60% to 30% also resulted in different timing and accumulation of denitrification products. The slow oxic

growth of both *At* and *Pd* hotspots due to the substrate diffusion limitation at 30% WFPS provided more time for *Pd* hotspots to interact with *At* hotspots than in the 60% WFPS treatment. Indeed, the NO burst from *At* hotspots after complete O₂ exhaustion in the random architecture was 50% higher at 30% WFPS indicating higher *At* cell numbers due to prolonged oxic growth (Figure 4c), whereas the N₂O peak was 50% lower, due to concomitant N₂O reduction in *Pt* hotspots (Figure 4d).

3.4. Mass balances

By the end of the incubation, oxygen was exhausted in all treatments. Likewise, NO₃⁻ was consumed by all treatments, except for the layered hotspots at 30% and 60% WFPS. This means that respiration was electron acceptor limited and that the cumulated recovery of denitrification products can be compared with the amount of NO₃⁻ initially present (Figure S8). The balance between aerobic and anaerobic respiration, e_{denit}^-/e_{total}^- (Bergau et al., 2011), is given by the electron flow to nitrogenous electron acceptors relative to the total electron flow, including O₂ respiration (Figure 5). When seen over all three water saturations, early stage denitrification under oxic headspace conditions (Figure 5a) showed a threshold response to increasing moisture with disproportionately higher e_{denit}^-/e_{total}^- ratios at 90% WFPS (17-27%) than at 60% or 30%. The proportions of electrons diverted to denitrification at low and medium saturations were small (2-7%) and even smaller than those observed in unconstrained hotspots (7-13%). Differences between saturations were less pronounced when the entire incubation period is considered (Figure 5b), since fully anoxic conditions during late stage incubation overrode saturation effects. Overall, the effect of hotspot architecture on e_{denit}^-/e_{total}^- ratios was smaller than the effect of saturation.

320 This stands in stark contrast to the pronounced effect of hotspot architecture on denitrification
product ratios (**Figure 5c, d**). Hotspot architecture governed growth rates through local
competition for O_2 and therewith the number of active cells involved in net production sites (*At*
hotspots) and net consumption sites (*Pd* hotspots) of NO once O_2 was exhausted. In layered
hotspot architectures there was hardly any net-release of NO to the headspace irrespective of
325 saturation (**Figure 5c**). With random hotspot architecture, there was substantial NO release, the
magnitude of which, however, decreased linearly with saturation. This pattern in NO
stoichiometry clearly reflects the number of *At* cells at the moment of complete O_2 depletion, as
affected by oxic growth which lasted longer with lower saturation. The N_2O product ratio (**Figure**
5d) was influenced by both saturation and hotspot architecture. In layered architectures, the N_2O
330 ratio increased exponentially with increasing saturation similar to what was observed for relative
electron flow to denitrification (**Figure 5a**). In random architectures, the N_2O product ratio was
consistently higher than in layered architectures irrespective of saturation, yet the highest ratio
was reached at 60% WFPS, due to the most vigorous growth, and hence fastest oxic-anoxic
transition at intermediate saturation.

335 [Figure 5]

3.5. Pore space properties

At the lowest saturation (30% WFPS), the entire air-filled pore space was connected to the
headspace (**Figure 6a**) and tortuosity was close to unity, i.e. the diffusion lengths in air only
depended on the vertical distance to the headspace (**Figure 6b**). The diffusion distances in water-
340 filled pores (**Figure 6c**) corresponded to the size of small, evenly distributed water clusters. At
medium saturation (60% WFPS), the amount of disconnected air was still negligible and
tortuosity only slightly increased. The increase in air distance was due to a few large water

pockets, which were caused by the step-wise addition of water to the repacked sand. Only at 90% saturation a considerable air volume of 5-20% became disconnected from the headspace. The path along which the remaining air was connected to the headspace became more tortuous with increasing saturation and average diffusion distances in water to the connected air cluster increased to 1 mm. This is still surprisingly short as compared to the size of the hotspots (7 mm). Independent tests showed that the high air connectivity at this low air content was facilitated by vacuum application during He/O₂-purging prior to the incubation. Directly after packing, the continuous air cluster only reached 10-15 mm into the sand (data not shown), whereas bubbling due to vacuum application formed continuous air channels that reached deep into the sand matrix connecting even the deepest hotspots with the headspace. Moreover, some larger gaps remained around hotspots during packing which tended to be air-filled after wetting. This is reflected in the consistently higher air-connectivity, lower air tortuosity and lower air distance, when only pores in the direct vicinity of hotspots are analyzed (**Figure 6a-c**). More than 90% of hotspot surfaces still had a direct air-filled connection with the headspace at 90% WFPS (**Figure 6a**). Depth profiles of these pore space attributes are reported in **Fig. S2**.

[Figure 6]

4. Discussion

4.1. Physical constraints on denitrification kinetics

The experimental setup in this incubation study was designed to investigate physical constraints on microbial respiration in hotspots as affected by the interplay between gaseous diffusion through a sterile matrix and local competition for oxygen. For this, we compared different combinations of water saturation in the matrix and spatial distributions of hotspots, which led to

365 different physical constraints for the supply of hotspots with oxygen. As a consequence, oxic growth rates differed among treatments which had various implications on denitrification as summarized in a conceptual scheme (Figure 7).

[Figure 7]

Our setup is a coarse simplification of soil in which metabolic activity in hotspots not only
370 depends on oxygen supply, but also on diffusion of substrates from the matrix to the hotspots. As such, our experiment does not allow to draw direct conclusions about the functioning of hotspots in real soils. However, by placing denitrifiers and their substrates into hotspots, we considerably reduced the level of complexity and created a system that is amenable to studying the dynamic interrelations between denitrifier growth, oxygen consumption and induction of denitrification by
375 gas kinetics.

Soil N₂O emissions are known to be highly variable in time and a unifying concept incorporating dynamic changes in denitrification activity and product stoichiometry in response to changing environmental conditions is still missing. Our model system provides a first data set for validating mathematical process models that are explicit for structural distribution of hotspots and
380 dynamic changes in boundary conditions (here mimicked by different hotspot architectures and declining oxygen concentrations in the headspace during batch incubation, respectively). The development of such models is a core activity of the DASIM project (<http://www.dasim.net/>). By combining metabolic measurements with advanced structural imaging and computation, we also provide a link to parameterizing such models with real soil data in future research.

385 Inoculating growing denitrifiers into porous glass beads and embedding them in sterile sand resulted in a highly dynamic system with respect to oxygen consumption and induction of denitrification. This was intended for the sake of experimental depth, but it must be noted that

oxic-anoxic transitions are likely slower, i.e. less dynamic in real-soil hotspots. In real soils, even highly organic hotspots contain a fair amount of recalcitrant organic C that limits microbial growth and oxygen consumption. Also with respect to denitrification stoichiometry, real soils may be expected to be less dynamic as multiple denitrifying phenotypes contained in the natural soil microbiome (Roco et al., 2017) utilize denitrification intermediates mutually. Notwithstanding, soil NO and N₂O emissions are known to be episodic in nature. Large, denitrification driven emission pulses occur upon abrupt changes in O₂ availability, caused by external factors like heavy rainfalls or soil freezing (Flessa et al., 1995), O₂ consumption by nitrification after ammoniacal fertilization (Huang et al., 2014) or incorporation of easily degradable organic matter (Flessa et al., 1995) which cannot be captured satisfactorily by common steady-state models for soil respiration and N₂O emission (Parton et al., 2001; Li et al., 1992). Even though the concept of hotspots is central in the understanding of denitrification dynamics in upland soils, common soil denitrification models do not account for the dynamics of spatially explicit hotspots in the soil matrix but rather scale bulk denitrification with a generic anoxic volume fraction (Li et al., 2000; Blagodatsky et al., 2011). To advance soil denitrification models, it is obvious that microbial respiration dynamics in hotspots have to be targeted, both conceptually (Wang et al., 2019) and experimentally (Kravchenko et al., 2017; Ebrahimi and Or, 2018). Our study is a first step in this direction.

One of the main findings of this study is that soil microbial respiration and the propensity to develop denitrifying anoxic hotspots does depend on their distribution in space. The onset of denitrification and its kinetics were linked to the spatial and temporal extent of anoxia developing in hotspot centers, which was governed by the interplay between denitrifier growth, diffusional constraints and hotspot architecture. When distributed randomly, microbial activity was most disperse relative to available oxygen, resulting in more growth, faster O₂ draw down and earlier

anoxia than when packed densely in layers (**Figure 3**). Rapid oxic-anoxic transition led to higher release rates of denitrification intermediates and increased NO and N₂O product ratios(**Figure 5c-d**). This effect was most pronounced at low and intermediate saturations but was dampened at 415 90%WFPS because oxygen supply was impeded by bulk diffusion irrespective of hotspot placement. Thus, our results highlight the significance of hotspot distribution at low soil moistures and exemplifies why N₂O emissions are notoriously difficult to predict under these conditions.

Even though we failed to fully synchronize *At* and *Pd* growth in time, our experiment 420 demonstrates that contrasting denitrification phenotypes may interact in modulating N₂O flux to the atmosphere. *Pd* hotspots reduced N₂O released from *At* hotspots irrespective of the layers' orientation (**Figure 3d**), which can be attributed to the high degree of air connectivity in the sand column (**Figure 1d**). We had expected more N₂O reduction with *Pd* on top (layered *Pd/At*), but since *At* grew faster than *Pd*, partial anoxia and NO and N₂O formation was induced in *At*, long 425 before N₂O consuming activity was induced in *Pd* hotspots. Future experiments with artificial hotspots should therefore carefully consider potential growth rates and air connectivity in packed soil.

4.2. Physical constraints on cumulative denitrification

The cumulative release of gaseous denitrification products, as described by electron flow ratios, 430 depended less on hotspot architecture than on soil moisture. Electron flows to denitrification ranged from <5% of total respiratory flow at low to medium saturations (30, 60% WFPS) to almost 23% at 90% WFPS (**Figure 5a**). We attribute the generally low denitrification electron flow in our experiments to the small active volume relative to the sterile sand matrix (the total volume fraction of hotspots was 14%, less of which was actually anoxic) and the large amount of

435 oxygen initially present in the incubation jars. Yet, we found a typical, non-linear denitrification response to soil moisture (**Figure 5a**). This threshold behavior is well known (Weier et al., 1993) and has been attributed to a disproportional contribution of small pores to the anoxic volume at higher saturation (Schurgers et al., 2006). In our system, consisting of coarse sand with a relatively homogenous pore size distribution, we attribute the non-linear response to an increase
440 in tortuosity of air-filled pores and an increase in distance to the next continuous air-filled pore that were pronounced enough to impair the oxygen supply to hotspots. Air connectivity, also increased non-linearly, but did not reach a critical value (**Figure 6**), ruling out that differences in NO and N₂O release at different saturations were due to gas entrapment but rather due to elongated diffusion pathways in air-filled and water-filled pores, leading to longer residence
445 times of denitrification intermediates and stronger reduction of intermediates in hotspots along the way to the headspace.

We cannot rule out bacterial spread out of the hotspots and that some denitrification might have occurred in the sand matrix. Nitrate and dissolved carbon diffused out of the hotspots and in addition at the lowest saturation (30%WFPS) those substrates were transported convectively by
450 capillary forces. This was demonstrated with a separate dye experiment (Figure S7). The fact that oxygen consumption was slow at 30%WFPS is indirect evidence that most bacteria remained in the hotspots. In other words, under well-aerated conditions only substrate limitation can explain a reduction in microbial growth as compared to the 60%WFPS and this can only occur if the substrates left the hotspots, but the cells did not follow to the same degree. For the 60% and
455 90%WFPS cases it is unclear as to how bacterial dispersal is really relevant. *A. tumefaciens* is known to possess flagella (Merritt et al., 2007), but *P. denitrificans* is not motile. Experimental data on bacterial dispersal rates in soil is scarce. In a recent study with *Bacillus subtilis* and *Pseudomonas fluorescens* inoculated to repacked soils at similar bulk density (1.5g/cm³) and

saturation (60%) the first cells appeared in a distance of 15mm after nine days (Juyal et al., 2018).

460 In our experiment, with the highest substrate concentration and the largest internal surface area in the hotspots denitrification occurred after 3-6 days. Hence, some cells may have colonized the immediate vicinity of hotspots, but cell densities outside the hotspots were likely low.

Saturation-dependent threshold behavior for denitrification is a well-studied phenomenon in soils (Linn and Doran, 1984;Ruser et al., 2006;Paul et al., 2003), but for a lack of pore scale
465 measurements often attributed to reduced bulk soil diffusivity. In undisturbed soil, the relative importance of air connectivity and distances between air-filled and water-filled pores might be more relevant for impairing oxygen supply and inducing denitrification. Air connectivity to the headspace was shown to affect N₂O emissions in terms of magnitude and responsiveness in repeated wetting/drying cycles in an intact soil column (Rabot et al., 2015). In agricultural soil
470 with different crop rotations, N₂O emissions were shown to correlate positively with the volume fraction of soil with macropore distances larger than 180 μm, which was used as an *ad-hoc* definition for poorly aerated soil (Kravchenko et al., 2018). In a mesocosm study on microstructural drivers for local redox conditions, none of the investigated soil pore metrics derived from X-ray CT data (excluding those examined here) correlated with redox kinetics
475 during a wetting/drying cycle (Wanzek et al., 2018). Hence, combining metabolic monitoring by high-resolution gas kinetics with direct assessment of diffusion lengths of gaseous and dissolved oxygen and denitrification products via X-ray microtomography emerges as a promising tool to study physical constraints for aerobic and anaerobic respiration in soil. However, meaningful metrics derived from X-ray data relevant for denitrification are yet to be developed and will
480 require additional experiments with both artificial and real soils. Improved understanding of factors and mechanisms controlling denitrification and N gas emission on a three-dimensional micro-scale may help to design and test soil management strategies that mediate the return of

excess nitrogen to the atmosphere in a controlled way, i.e. with as little as possible NO and N₂O release, be it by crop residue (Kravchenko et al., 2017), pH (Russenet et al., 2016) or irrigation (Bergstermann et al., 2011) management. At the same time, our experiments call for the implementation of spatially explicit reaction-diffusion algorithms (Hron et al., 2015; Ebrahimi and Or, 2016) in soil process models. For instance, diffusion lengths between hotspots and air-filled pores connected to the headspace may serve as a useful metric to be implemented on model concepts like the anaerobic soil volume fraction in larger-scale continuum models (Li et al., 2000; Schurgers et al., 2006; Blagodatsky et al., 2011).

5. Conclusions

Using a highly simplified model system, we demonstrate that the denitrification in heterogeneous media like soil critically depends on water saturation as well as on the spatial distribution of microbial hotspots. Hotspot architecture effects were particularly pronounced with respect to denitrification stoichiometry resulting in vastly different NO and N₂O release rates. Even though our experiment was conducted in a closed system, with growing denitrifier strains and a limited amount of substrate, the results are relevant for real soils in that they represent a benchmark scenario of hotspot-driven denitrification. More importantly, our reductionist approach resulted in an experimental dataset that is amenable to process-based, pore-scale denitrification models, which will be the subject of a future study.

Hotspot architecture played a more pronounced role for denitrification kinetics at lower soil moisture (30 and 60% WFPS). Hence, denitrification and its gaseous product stoichiometry do not only depend on the amount of microbial hotspots in aerated soil, but also on their spatial distribution. The total amount of denitrification measured as cumulative electron flow, in turn, depended more on water saturation which is in line with the well-known saturation-dependent

threshold behavior in denitrification also found in natural soil. For the case of artificial soil used in our study, we found that this threshold behavior was best explained by increased air tortuosity and air distance at high saturations. Future experiments with artificial and natural soils are needed to fully capture the regulation of denitrification at the micro-scale.

510 **6. Data availability**

All segmented X-ray μ CT files and the GC data are permanently available through the UFZ archive with data description using standardized metadata catalogue (Dublin Core) and with access via URL: <http://www.ufz.de/record/<to-be-filled-after-acceptance>>.

7. Author contribution

515 SS, HV and PD designed the experiments. SS, JZ and PD carried them out. SS, JZ and PD processed the data. SS prepared the manuscript with contributions from all co-authors.

8. Competing interests

The authors declare that they have no conflict of interest.

9. Acknowledgments

520 We thank Ali Ebrahimi and an anonymous reviewer for the constructive comments. This study was funded by the Deutsche Forschungsgemeinschaft through the research unit DFG-FOR 2337: Denitrification in Agricultural Soils: Integrated Control and Modelling at Various Scales (DASIM). PD received funding from the FACCE-ERA-GAS project MAGGE-pH under the Grant Agreement No. 696356. We thank Linda Bergaust for providing the bacterial strains, Jing

525 Zhu for laboratory support and Olaf Ippisch and Marcus Horn for helpful discussions during the planning of the experiment.

10. References

528 Arah, J. R. M., and Vinten, A. J. A.: Simplified models of anoxia and denitrification in
529 aggregated and simple-structured soils, *European Journal of Soil Science*, 46, 507-517, DOI
530 10.1111/j.1365-2389.1995.tb01347.x, 1995.

531 Ball, B. C.: Soil structure and greenhouse gas emissions: a synthesis of 20 years of
532 experimentation, *European Journal of Soil Science*, 64, 357-373, 10.1111/ejss.12013, 2013.

533 Bergaust, L., Shapleigh, J., Frostegard, A., and Bakken, L.: Transcription and activities of NOx
534 reductases in *Agrobacterium tumefaciens* : The influence of nitrate, nitrite and oxygen
535 availability, *Environ. Microbiol.*, 10, 3070-3081, 2008.

536 Bergaust, L., Mao, Y., Bakken, L., and Frostegard, A.: Denitrification response patterns during
537 the transition to anoxic respiration and posttranscriptional effects of suboptimal pH on nitrogen
538 oxide reductase in *Paracoccus denitrificans* *Appl. Environ. Microbiol.*, 76, 6387-6396, 2010.

539 Bergaust, L., Bakken, Lars R., and Frostegård, A.: Denitrification regulatory phenotype, a new
540 term for the characterization of denitrifying bacteria, *Biochemical Society Transactions*, 39, 207-
541 212, 10.1042/bst0390207, 2011.

542 Bergstermann, A., Cárdenas, L., Bol, R., Gilliam, L., Goulding, K., Meijide, A., Scholefield, D.,
543 Vallejo, A., and Well, R.: Effect of antecedent soil moisture conditions on emissions and
544 isotopologue distribution of N2O during denitrification, *Soil Biology and Biochemistry*, 43, 240-
545 250, <https://doi.org/10.1016/j.soilbio.2010.10.003>, 2011.

546 Blagodatsky, S., Grote, R., Kiese, R., Werner, C., and Butterbach-Bahl, K.: Modelling of
547 microbial carbon and nitrogen turnover in soil with special emphasis on N-trace gases emission,
548 *Plant and Soil*, 346, 297, 10.1007/s11104-011-0821-z, 2011.

549 Doube, M., Kłosowski, M. M., Arganda-Carreras, I., Cordelières, F. P., Dougherty, R. P.,
550 Jackson, J. S., Schmid, B., Hutchinson, J. R., and Shefelbine, S. J.: BoneJ: Free and extensible
551 bone image analysis in *ImageJ*, *Bone*, 47, 1076-1079, 2010.

552 Ebrahimi, A., and Or, D.: Microbial community dynamics in soil aggregates shape
553 biogeochemical gas fluxes from soil profiles - upscaling an aggregate biophysical model, *Global
554 Change Biology*, 22, 3141-3156, 2016.

555 Ebrahimi, A., and Or, D.: Dynamics of soil biogeochemical gas emissions shaped by remolded
556 aggregate sizes and carbon configurations under hydration cycles, *Global Change Biology*, 24,
557 e378-e392, 10.1111/gcb.13938, 2018.

558 Elberling, B., Askaer, L., Jørgensen, C. J., Joensen, H. P., Köhl, M., Glud, R. N., and Lauritsen,
559 F. R.: Linking Soil O2, CO2, and CH4 Concentrations in a Wetland Soil: Implications for CO2
560 and CH4 Fluxes, *Environmental Science & Technology*, 45, 3393-3399, 10.1021/es103540k,
561 2011.

562 Flessa, H., Dörsch, P., and Beese, F.: Seasonal variation of N2O and CH4 fluxes in differently
563 managed arable soils in southern Germany, *Journal of Geophysical Research: Atmospheres*, 100,
564 23115-23124, doi:10.1029/95JD02270, 1995.

565 Groffman, P. M., Butterbach-Bahl, K., Fulweiler, R. W., Gold, A. J., Morse, J. L., Stander, E. K.,
566 Tague, C., Tonitto, C., and Vidon, P.: Challenges to incorporating spatially and temporally
567 explicit phenomena (hotspots and hot moments) in denitrification models, *Biogeochemistry*, 93,
568 49-77, 2009.

569 Højberg, O., Revsbech, N. P., and Tiedje, J. M.: Denitrification in soil aggregates analyzed with
570 microensors for nitrous oxide and oxygen, *Soil Science Society of America Journal*, 58, 1691-
571 1698, 1994.

572 Horn, R., Stepniewski, W., Włodarczyk, T., Walenzik, G., and Eckhardt, F.: Denitrification rate
573 and microbial distribution within homogeneous model soil aggregates, *Int. Agrophysics*, 8, 65-
574 74, 1994.

575 Hron, P., Jost, D., Bastian, P., Gallert, C., Winter, J., and Ippisch, O.: Application of Reactive
576 Transport Modeling to Growth and Transport of Microorganisms in the Capillary Fringe, *Vadose*
577 *Zone Journal*, 14, 10.2136/vzj2014.07.0092, 2015.

578 Huang, T., Gao, B., Hu, X.-K., Lu, X., Well, R., Christie, P., Bakken, L. R., and Ju, X.-T.:
579 Ammonia-oxidation as an engine to generate nitrous oxide in an intensively managed calcareous
580 Fluvo-aquic soil, *Scientific Reports*, 4, 3950, 10.1038/srep03950

581 <https://www.nature.com/articles/srep03950#supplementary-information>, 2014.

582 Juyal, A., Eickhorst, T., Falconer, R., Baveye, P. C., Spiers, A., and Otten, W.: Control of Pore
583 Geometry in Soil Microcosms and Its Effect on the Growth and Spread of *Pseudomonas* and
584 *Bacillus* sp, *Frontiers in Environmental Science*, 6, 10.3389/fenvs.2018.00073, 2018.

585 Keiluweit, M., Wanzek, T., Kleber, M., Nico, P., and Fendorf, S.: Anaerobic microsites have an
586 unaccounted role in soil carbon stabilization, *Nature Communications*, 8, 1771, 10.1038/s41467-
587 017-01406-6, 2017.

588 Keiluweit, M., Gee, K., Denney, A., and Fendorf, S.: Anoxic microsites in upland soils
589 dominantly controlled by clay content, *Soil Biology and Biochemistry*, 118, 42-50,
590 <https://doi.org/10.1016/j.soilbio.2017.12.002>, 2018.

591 Kravchenko, A. N., Toosi, E. R., Guber, A. K., Ostrom, N. E., Yu, J., Azeem, K., Rivers, M. L.,
592 and Robertson, G. P.: Hotspots of soil N₂O emission enhanced through water absorption by plant
593 residue, *Nature Geoscience*, 10, 496, 10.1038/ngeo2963

594 <https://www.nature.com/articles/ngeo2963#supplementary-information>, 2017.

595 Kravchenko, A. N., Guber, A. K., Quigley, M. Y., Koestel, J., Gandhi, H., and Ostrom, N. E.: X-
596 ray computed tomography to predict soil N₂O production via bacterial denitrification and N₂O
597 emission in contrasting bioenergy cropping systems, *GCB Bioenergy*, 0,
598 doi:10.1111/gcbb.12552, 2018.

599 Kuzyakov, Y., and Blagodatskaya, E.: Microbial hotspots and hot moments in soil: Concept &
600 review, *Soil Biology and Biochemistry*, 83, 184-199, 2015.

601 Legland, D., Arganda-Carreras, I., and Andrey, P.: MorphoLibJ: integrated library and plugins
602 for mathematical morphology with ImageJ, *Bioinformatics*, 32, 3532-3534, 2016.

603 Li, C., Frolking, S., and Frolking, T. A.: A model of nitrous oxide evolution from soil driven by
604 rainfall events: 1. Model structure and sensitivity, *Journal of Geophysical Research:*
605 *Atmospheres*, 97, 9759-9776, doi:10.1029/92JD00509, 1992.

606 Li, C., Aber, J., Stange, F., Butterbach-Bahl, K., and Papen, H.: A process-oriented model of
607 N₂O and NO emissions from forest soils: 1. Model development, *Journal of Geophysical*
608 *Research: Atmospheres*, 105, 4369-4384, 2000.

609 Linn, D., and Doran, J.: Effect of water-filled pore space on carbon dioxide and nitrous oxide
610 production in tilled and nontilled soils, *Soil Science Society of America Journal*, 48, 1267-1272,
611 1984.

612 Mangalassery, S., Sjögersten, S., Sparkes, D. L., Sturrock, C. J., and Mooney, S. J.: The effect of
613 soil aggregate size on pore structure and its consequence on emission of greenhouse gases, *Soil*
614 *and Tillage Research*, 132, 39-46, <https://doi.org/10.1016/j.still.2013.05.003>, 2013.

615 Mathieu, O., Lévêque, J., Hénault, C., Milloux, M.-J., Bizouard, F., and Andreux, F.: Emissions
616 and spatial variability of N₂O, N₂ and nitrous oxide mole fraction at the field scale, revealed with
617 ¹⁵N isotopic techniques, *Soil Biology and Biochemistry*, 38, 941-951, 2006.

618 Merritt, P. M., Danhorn, T., and Fuqua, C.: Motility and chemotaxis in *Agrobacterium*
619 *tumefaciens* surface attachment and biofilm formation, *J Bacteriol*, 189, 8005-8014,
620 10.1128/JB.00566-07, 2007.

621 Miller, M. N., Zebarth, B. J., Dandie, C. E., Burton, D. L., Goyer, C., and Trevors, J. T.:
622 Denitrifier Community Dynamics in Soil Aggregates under Permanent Grassland and Arable
623 Cropping Systems, *Soil Science Society of America Journal*, 73, 1843-1851,
624 10.2136/sssaj2008.0357, 2009.

625 Molstad, L., Dörsch, P., and Bakken, L. R.: Robotized incubation system for monitoring gases
626 (O₂, NO, N₂O, N₂) in denitrifying cultures, *Journal of Microbiological Methods*, 71, 202-211,
627 2007.

628 Moyano, F. E., Vasilyeva, N., Bouckaert, L., Cook, F., Craine, J., Curiel Yuste, J., Don, A.,
629 Epron, D., Formanek, P., Franzluebbers, A., Ilstedt, U., Kätterer, T., Orchard, V., Reichstein, M.,
630 Rey, A., Ruamps, L., Subke, J. A., Thomsen, I. K., and Chenu, C.: The moisture response of soil
631 heterotrophic respiration: interaction with soil properties, *Biogeosciences*, 9, 1173-1182,
632 10.5194/bg-9-1173-2012, 2012.

633 Nunan, N.: The microbial habitat in soil: Scale, heterogeneity and functional consequences,
634 *Journal of Plant Nutrition and Soil Science*, 180, 425-429, 10.1002/jpln.201700184, 2017.

635 Parkin, T. B.: Soil microsites as a source of denitrification variability, *Soil Science Society of*
636 *America Journal*, 51, 1194-1199, 1987.

637 Parry, S., Renault, P., Chenu, C., and Lensi, R.: Denitrification in pasture and cropped soil clods
638 as affected by pore space structure, *Soil Biology and Biochemistry*, 31, 493-501,
639 [https://doi.org/10.1016/S0038-0717\(98\)00101-1](https://doi.org/10.1016/S0038-0717(98)00101-1), 1999.

640 Parton, W. J., Holland, E. A., Del Grosso, S. J., Hartman, M. D., Martin, R. E., Mosier, A. R.,
641 Ojima, D. S., and Schimel, D. S.: Generalized model for NO_x and N₂O emissions from soils,
642 *Journal of Geophysical Research: Atmospheres*, 106, 17403-17419, doi:10.1029/2001JD900101,
643 2001.

644 Paul, K. I., Polglase, P. J., O'Connell, A. M., Carlyle, J. C., Smethurst, P. J., and Khanna, P. K.:
645 Defining the relation between soil water content and net nitrogen mineralization, *European*
646 *Journal of Soil Science*, 54, 39-48, doi:10.1046/j.1365-2389.2003.00502.x, 2003.

647 Rabot, E., Lacoste, M., Hénault, C., and Cousin, I.: Using X-ray Computed Tomography to
648 Describe the Dynamics of Nitrous Oxide Emissions during Soil Drying, *Vadose Zone Journal*,
649 14, 10.2136/vzj2014.12.0177, 2015.

650 Risk, N., Wagner-Riddle, C., Furon, A., Warland, J., and Blodau, C.: Comparison of
651 Simultaneous Soil Profile N₂O Concentration and Surface N₂O Flux Measurements Overwinter
652 and at Spring Thaw in an Agricultural Soil, *Soil Science Society of America Journal*, 78, 180-
653 193, 10.2136/sssaj2013.06.0221, 2014.

654 Roco, C. A., Bergaust, L. L., Bakken, L. R., Yavitt, J. B., and Shapleigh, J. P.: Modularity of
655 nitrogen-oxide reducing soil bacteria: linking phenotype to genotype, *Environmental*
656 *Microbiology*, 19, 2507-2519, doi:10.1111/1462-2920.13250, 2017.

657 Röver, M., Heinemeyer, O., Munch, J. C., and Kaiser, E.-A.: Spatial heterogeneity within the
658 plough layer: high variability of N₂O emission rates, *Soil Biology and Biochemistry*, 31, 167-
659 173, 1999.

660 Ruser, R., Flessa, H., Russow, R., Schmidt, G., Buegger, F., and Munch, J. C.: Emission of N₂O,
661 N₂ and CO₂ from soil fertilized with nitrate: effect of compaction, soil moisture and rewetting,
662 *Soil Biology and Biochemistry*, 38, 263-274, <https://doi.org/10.1016/j.soilbio.2005.05.005>, 2006.

663 Russenes, A. L., Korsæth, A., Bakken, L. R., and Dörsch, P.: Spatial variation in soil pH controls
664 off-season N₂O emission in an agricultural soil, *Soil Biology and Biochemistry*, 99, 36-46,
665 <https://doi.org/10.1016/j.soilbio.2016.04.019>, 2016.

666 Russenes, A. L., Korsæth, A., Bakken, L. R., and Dörsch, P.: Effects of nitrogen split application
667 on seasonal N₂O emissions in southeast Norway, *Nutrient Cycling in Agroecosystems*,
668 10.1007/s10705-019-10009-0, 2019.

669 Schaufler, G., Kitzler, B., Schindlbacher, A., Skiba, U., Sutton, M. A., and Zechmeister-
670 Boltenstern, S.: Greenhouse gas emissions from European soils under different land use: effects
671 of soil moisture and temperature, *European Journal of Soil Science*, 61, 683-696, 10.1111/j.1365-
672 2389.2010.01277.x, 2010.

673 Schindelin, J., Arganda-Carreras, I., Frise, E., Kaynig, V., Longair, M., Pietzsch, T., Preibisch,
674 S., Rueden, C., Saalfeld, S., and Schmid, B.: Fiji: an open-source platform for biological-image
675 analysis, *Nature methods*, 9, 676-682, 2012.

676 Schlüter, S., Sheppard, A., Brown, K., and Wildenschild, D.: Image processing of multiphase
677 images obtained via X-ray microtomography: A review, *Water Resources Research*, 50, 3615-
678 3639, 2014.

679 Schlüter, S., Henjes, S., Zawallich, J., Bergaust, L., Horn, M., Ippisch, O., Vogel, H.-J., and
680 Dörsch, P.: Denitrification in Soil Aggregate Analogues-Effect of Aggregate Size and Oxygen
681 Diffusion, *Frontiers in Environmental Science*, 6, 10.3389/fenvs.2018.00017, 2018.

682 Schurgers, G., Dorsch, P., Bakken, L., Leffelaar, P., and Haugen, L. E.: Modelling soil
683 anaerobiosis from water retention characteristics and soil respiration, *Soil Biology &
684 Biochemistry*, 38, 2637-2644, 10.1016/j.soilbio.2006.04.016, 2006.

685 Sexstone, A. J., Revsbech, N. P., Parkin, T. B., and Tiedje, J. M.: Direct measurement of oxygen
686 profiles and denitrification rates in soil aggregates, *Soil science society of America journal*, 49,
687 645-651, 1985.

688 Sierra, J., and Renault, P.: Respiratory Activity and Oxygen Distribution in Natural Aggregates in
689 Relation to Anaerobiosis, *Soil Science Society of America Journal*, 60, 1428-1438,
690 10.2136/sssaj1996.03615995006000050020x, 1996.

691 Sistrom, W. R.: A Requirement for Sodium in the Growth of *Rhodopseudomonas spheroides*,
692 *Microbiology*, 22, 778-785, 1960.

693 Smith, K. A.: A model of the extent of anaerobic zones in aggregated soils, and its potential
694 application to estimates of denitrification, *Journal of Soil Science*, 31, 263-277, 10.1111/j.1365-
695 2389.1980.tb02080.x, 1980.

696 Smith, K. A., Ball, T., Conen, F., Dobbie, K. E., Massheder, J., and Rey, A.: Exchange of
697 greenhouse gases between soil and atmosphere: interactions of soil physical factors and
698 biological processes, *European Journal of Soil Science*, 54, 779-791, 10.1046/j.1351-
699 0754.2003.0567.x, 2003.

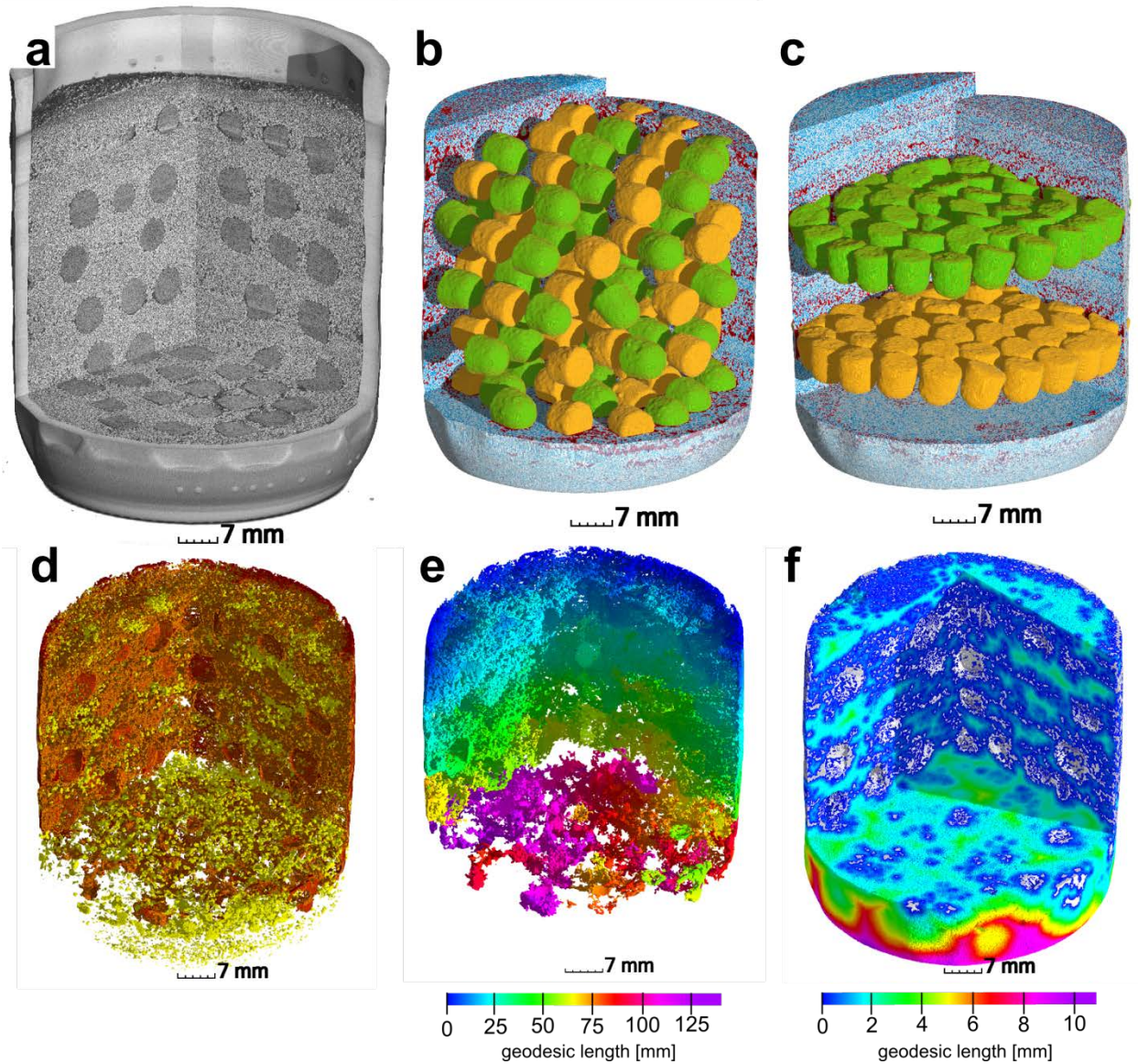
700 Tecon, R., and Or, D.: Biophysical processes supporting the diversity of microbial life in soil,
701 *FEMS Microbiology Reviews*, 41, 599-623, 10.1093/femsre/fux039, 2017.

702 Wang, B., Brewer, P. E., Shugart, H. H., Lerdau, M. T., and Allison, S. D.: Soil aggregates as
703 biogeochemical reactors and implications for soil-atmosphere exchange of greenhouse gases—A
704 concept, *Global Change Biology*, 0, doi:10.1111/gcb.14515, 2019.

705 Wanzek, T., Keiluweit, M., Varga, T., Lindsley, A., Nico, P. S., Fendorf, S., and Kleber, M.: The
706 Ability of Soil Pore Network Metrics to Predict Redox Dynamics is Scale Dependent, *Soil
707 Systems*, 2, 66, 2018.

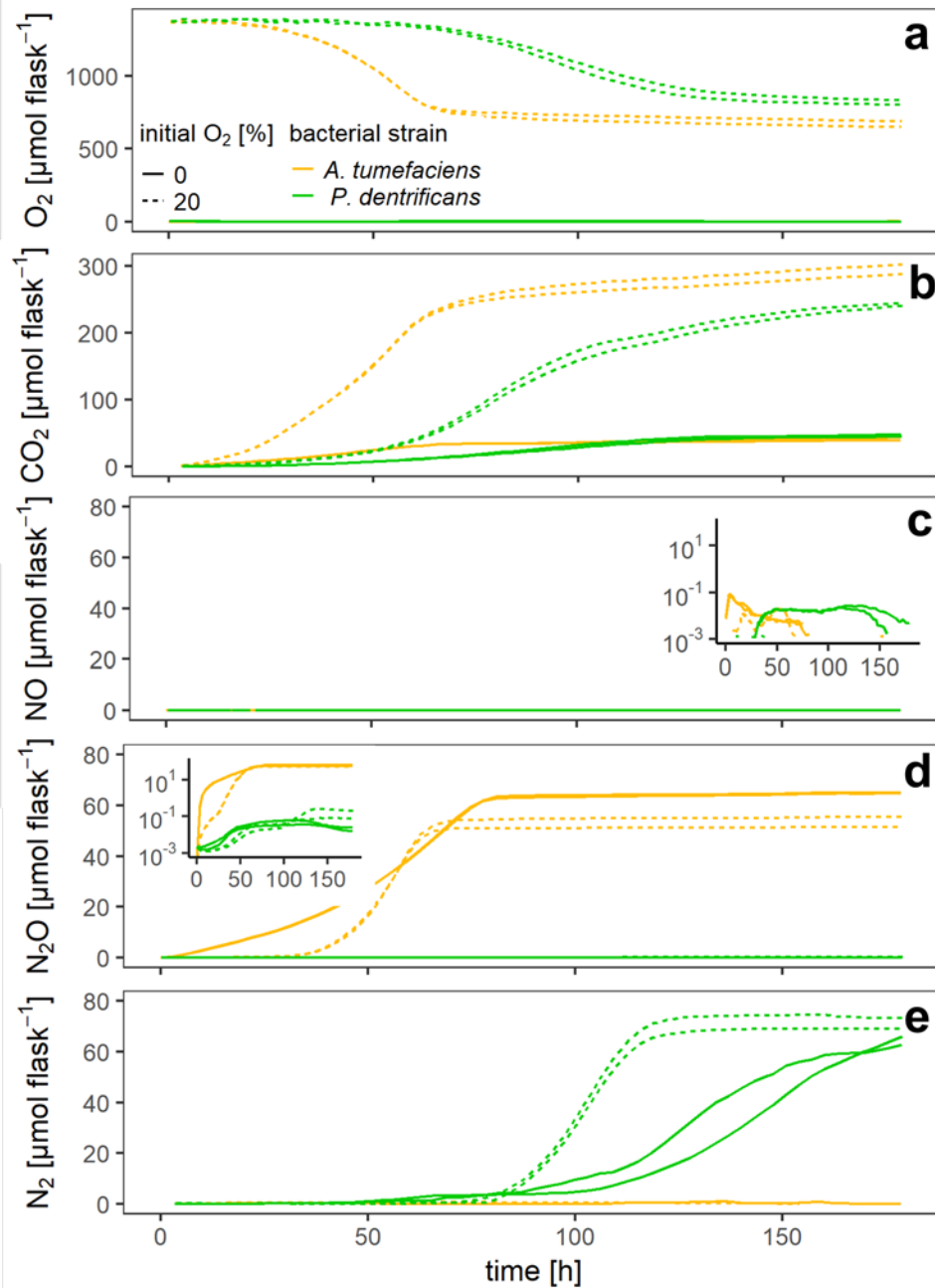
708 Weier, K. L., Doran, J. W., Power, J. F., and Walters, D. T.: Denitrification and the
709 Dinitrogen/Nitrous Oxide Ratio as Affected by Soil Water, Available Carbon, and Nitrate, *Soil
710 Science Society of America Journal*, 57, 66-72, 10.2136/sssaj1993.03615995005700010013x,
711 1993.

712 Zausig, J., Stepniewski, W., and Horn, R.: Oxygen Concentration and Redox Potential Gradients
713 in Unsaturated Model Soil Aggregates, *Soil Science Society of America Journal*, 57, 908-916,
714 10.2136/sssaj1993.03615995005700040005x, 1993.



716

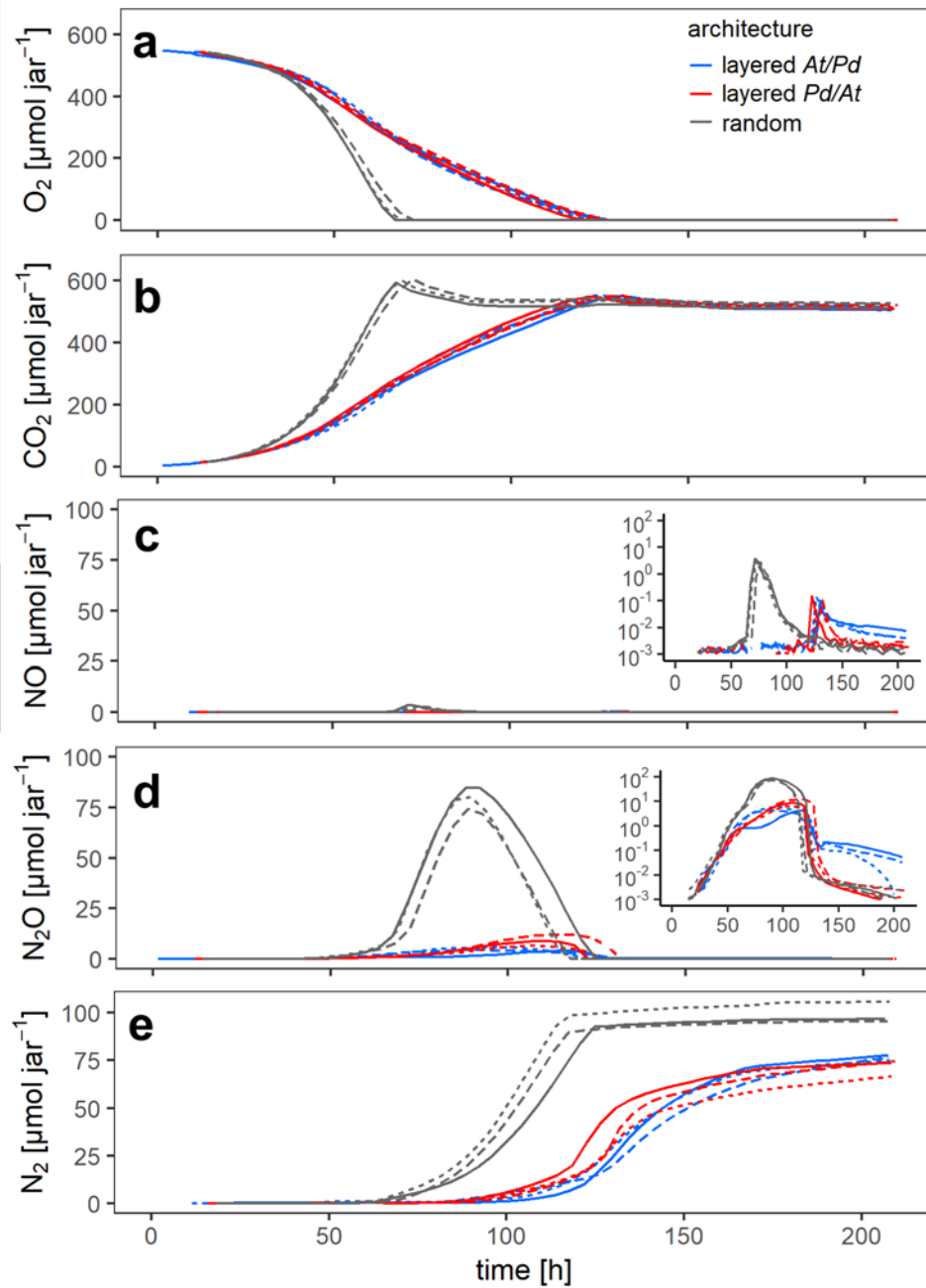
717 Figure 1. Upper panel: (a) X-ray CT scan of an incubation jar with random hotspot architecture and medium saturation
 718 (60% WFPS). (b) Image segmentation of the same jar into air (red), water (blue), sand (transparent), *A. tumefaciens*
 719 hotspots (orange) and *P. denitrificans* hotspots (green). (c) A different jar at medium saturation (60% WFPS) with layered
 720 *Pd/At* hotspot architecture. Lower panel: a jar with random distribution at high saturation (90% WFPS). (d) Air
 721 connectivity, determined as the volume fraction of air connected to the headspace (red, disconnected air shown in yellow).
 722 (e) Air tortuosity as derived from the geodesic length to the headspace within the connected air cluster. (f) Diffusion
 723 lengths determined as the geodesic length to the closest connected air cluster (white) within water-filled pores.



724

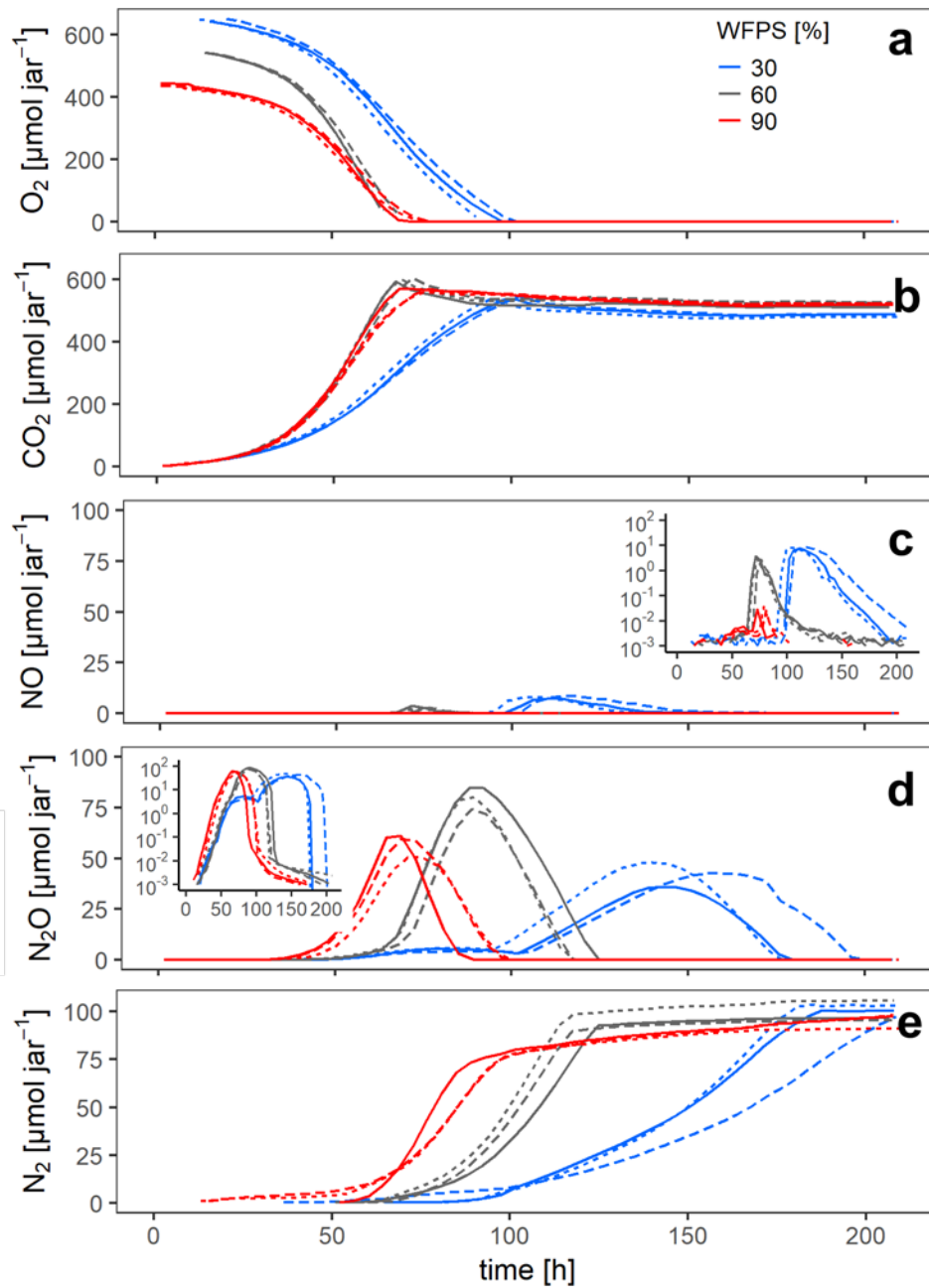
725
726
727
728

Figure 2: Gas kinetics of individual sets of hotspots that were loosely placed in empty flasks (fifty each), saturated with a growth medium and inoculated with two different bacterial strains – either a full denitrifier (*P. denitrificans*) or a truncated denitrifier lacking N₂O reductase (*A. tumefaciens*) - under oxic and anoxic conditions: (a) O₂, (b) CO₂, (c) NO, (d) N₂O, (e) N₂.



729

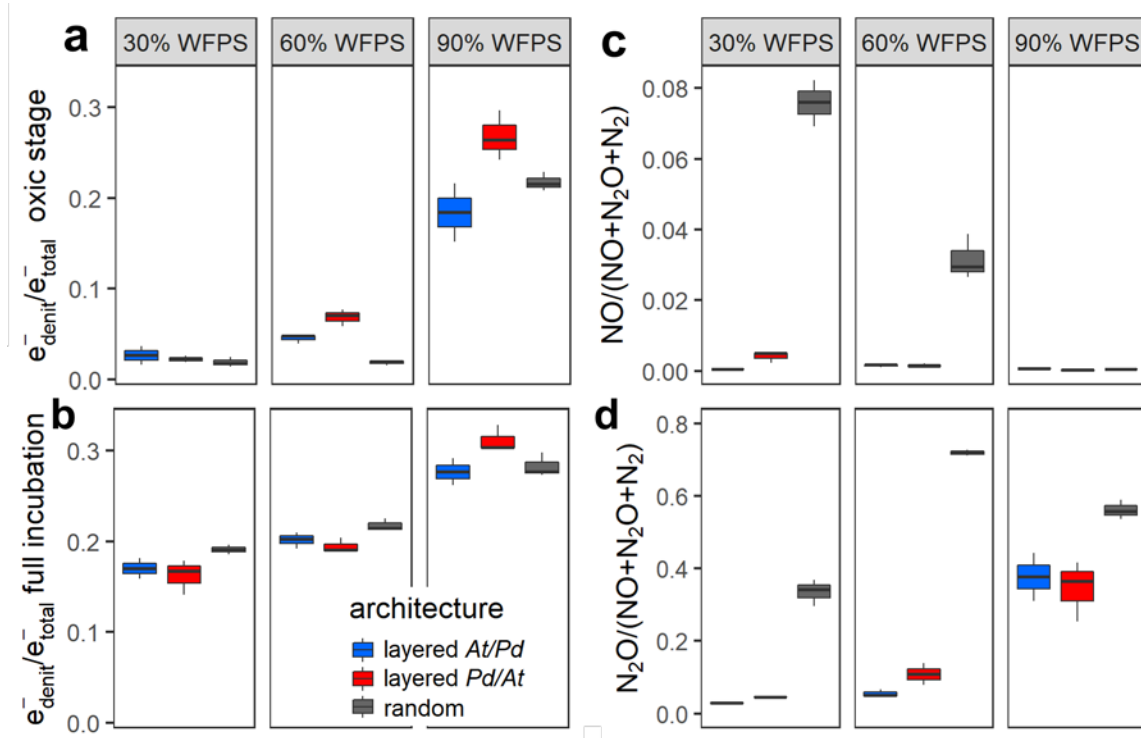
730 Figure 3: Gas kinetics in all treatments at medium saturation in the sand (60% WFPS) and an initial O₂ concentration of
 731 20% in the headspace for three different hotspot architectures containing a total of 100 hotspots, in which the hotspots
 732 either had maximum separation distance (random) or were densely packed in layers either with all At hotspots (layered
 733 At/Pd) or all Pd hotspots (layered Pd/At) in the upper layer : (a) O₂, (b) CO₂, (c) NO, (d) N₂O, (e) N₂. Data is only shown
 734 for the first 210h of the incubation period (300h total). Different lines styles represent replicates.



735

736
737

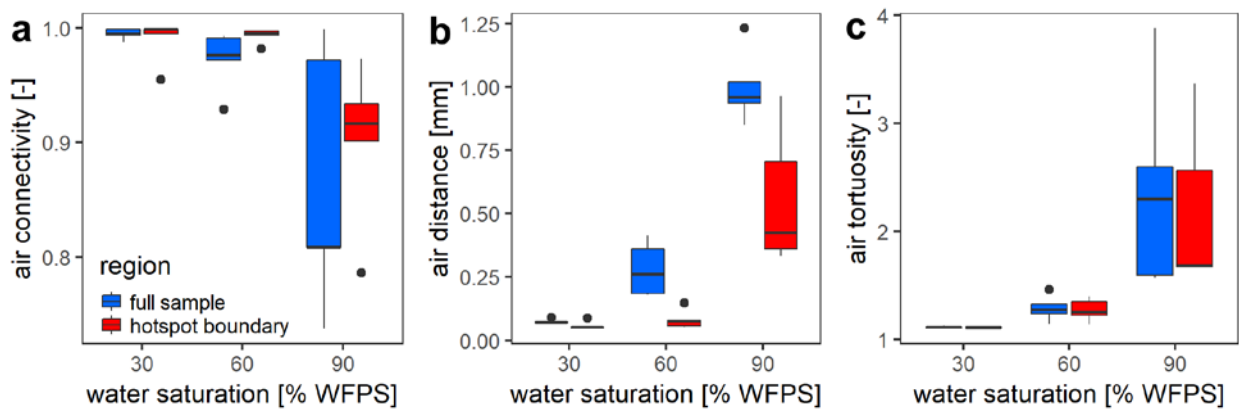
Figure 4: Gas kinetics of randomly placed hotspots at three different saturations in the sand and an initial O_2 concentration of 20% in the headspace: (a) O_2 , (b) CO_2 , (c) NO , (d) N_2O , (e) N_2 . Different lines styles represent replicates.



738

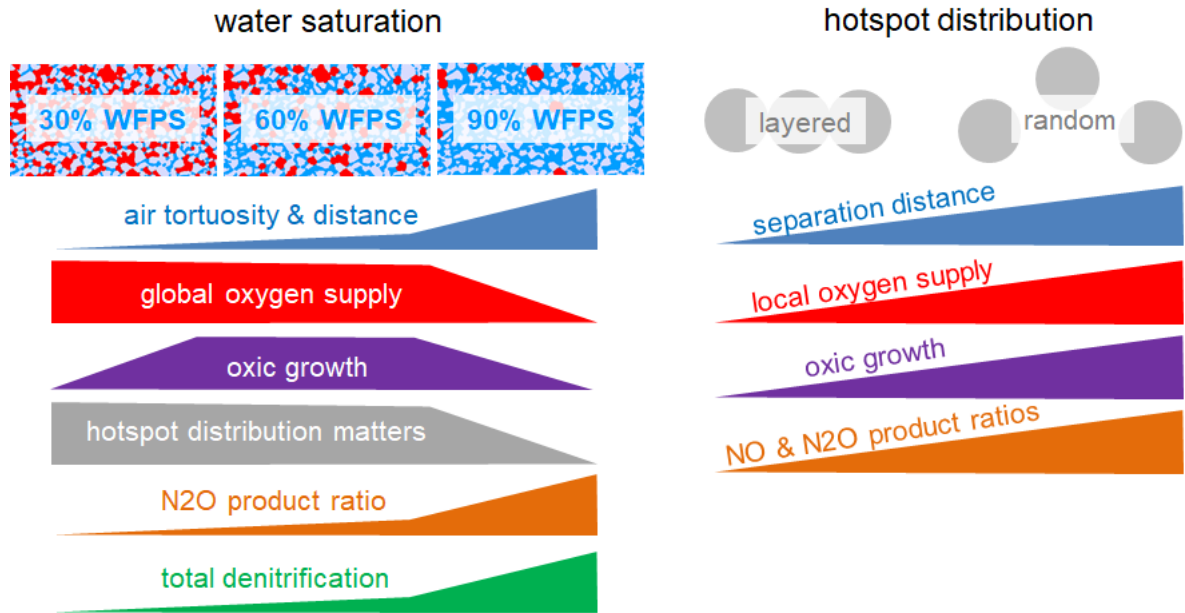
739 Figure 5: The proportion of denitrification in total respiration expressed as relative electron flow for all architectures and
 740 saturations. Values are reported for (a) the initial, oxic to hypoxic stage (O_2 present in headspace) and (b) for the full
 741 incubation period of 300 h. The product ratios for NO (c) and N_2O (d) consider the full incubation period and are
 742 corrected for the release of precursor gases. Data shown as box-whisker plots: Whiskers- min-max, middle lines - median.

743



744

745 Figure 6: Morphological properties of air-filled pores at different saturations averaged over different hotspots
 746 architectures ($n=5$). These properties are reported separately for the entire pore space within the region of interest (full
 747 sample) and for the pore space in direct vicinity to the porous glass beads (hotspot boundary): (a) air connectivity
 748 represents the volume fraction of air with direct connection to the headspace. (b) Air tortuosity represents the ratio
 749 between geodesic length to the headspace and Euclidean distance for any voxel within the connected air-cluster. (c) Air
 750 distance represents the geodesic distance to the connected air cluster within the water-filled pores. Data shown as box-
 751 whisker plots: Whiskers- min-max, middle lines – median, dots: outliers.



752

753

754

755

Figure 7: Summary of the experimental findings about the impact of water saturation and spatial hotspot distribution on the physical constraints on the supply of hotspots with oxygen, the resulting growth rates and the implication of various aspects of denitrification.

Physical constraints for respiration in microbial hotspots in soil and their importance for denitrification

Steffen Schlüter¹, Jan Zawallich², Hans-Jörg Vogel¹, Peter Dörsch³

¹ Department Soil System Sciences, Helmholtz-Centre for Environmental Research - UFZ,

5 Theodor-Lieser-Str. 4, 06120 Halle, Germany

² Institute of Mathematics, TU Clausthal, Erzstr. 1, Clausthal-Zellerfeld, Germany

³ Faculty of Environmental Sciences and Natural Resource Management, Norwegian University of Life Sciences, NMBU, Aas, Norway

correspondence to: Steffen Schlüter (steffen.schlueter@ufz.de)

10 **Abstract** Soil denitrification is the most important terrestrial process returning reactive nitrogen to the atmosphere, but remains poorly understood. In upland soils, denitrification occurs in hotspots of enhanced microbial activity, even under well-aerated conditions, and causes harmful emissions of nitric (NO) and nitrous oxide (N₂O). Timing and magnitude of such emissions are difficult to predict due to the delicate balance of oxygen (O₂) consumption and diffusion in soil.

15 To study how spatial distribution of hotspots affects O₂ exchange and denitrification, we embedded microbial hotspots composed of porous glass beads saturated with growing cultures of ~~inoculated with~~ either *Agrobacterium tumefaciens* (a denitrifier lacking N₂O reductase) or *Paracoccus denitrificans* (a "complete" denitrifier) in different architectures (random vs. layered) in sterile sand that was adjusted to different water saturations (30%, 60%, 90%) ~~and measured~~

20 G_gas kinetics (O₂, CO₂, NO, N₂O and N₂) were measured at high temporal resolution in batch mode. -Air connectivity, air distance and air tortuosity were determined by X-ray tomography after the experiment. The hotspot architecture exerted strong control on microbial growth and timing of denitrification at low and intermediate saturations, because the separation distance between the microbial hotspots governed local oxygen supply. Electron flow diverted to

25 denitrification in anoxic hotspot centers was low (2-7%) but increased markedly (17-27%) at high
water saturation. X-ray analysis revealed that the air phase around most of the hotspots remained
connected to the headspace even at 90% saturation, suggesting that the threshold response of
denitrification to soil moisture could be ascribed ~~solely~~ to increasing tortuosity of air-filled pores
and the distance from the saturated hotspots to these air-filled pores. Our findings suggest that
30 denitrification and its gaseous product stoichiometry do not only depend on the amount of
microbial hotspots in aerated soil, but also on their spatial distribution. We demonstrate that
combining measurements of microbial activity with quantitative analysis of diffusion lengths
using X-ray tomography provides unprecedented insights into physical constraints regulating soil
microbial respiration in general and denitrification in particular. This ~~opens new avenues~~
35 paves the way to using observable soil structural attributes to predict denitrification and to
parameterize models. ~~Further experiments with natural soil structure, carbon substrates and
microbial communities are required to demonstrate this under realistic conditions~~
devise and
parametrize denitrification models explicit for microbial hotspots.

1. Introduction

40 Soil carbon and nitrogen turnover is governed by soil heterogeneity at the microscale. Much of
the turnover is concentrated in microsites, providing favorable conditions (pO_2 , temperature, pH)
and substrates (carbon, nutrients) for soil microbial activity. The partitioning of aerobic and
anaerobic respiration in microsites is largely controlled by the water content in the soil matrix
which defines the scale across which O_2 diffuses towards microsites of high O_2 -consuming
45 activity. Aqueous diffusion lengths range from distances across thin water films in well-aerated
soils, to individual soil aggregates of different radii at field capacity, up to the distance to the soil
surface when the soil is saturated (Smith et al., 2003; Elberling et al., 2011; Ball, 2013; Parkin,

1987). Aerobic respiration is less affected by soil moisture than anaerobic respiration and typically peaks around water saturations of 20-60% ~~in forest, grass and cropland soils~~ (Schaufler et al., 2010; Ruser et al., 2006; Moyano et al., 2012). Bulk soil respiration starts to decline at higher saturations due to the development of anoxic microsites with lower redox potential, supporting carbon mineralization at typically only a tenth of the rates observed under oxic conditions (Keiluweit et al., 2017). Denitrification, i.e. the dissimilatory respiration of N oxyanions instead of oxygen, is commonly observed at water saturations above 60-70% and peaks beyond 90% (Ruser et al., 2006; Linn and Doran, 1984). The occurrence of anaerobic microsites is governed by the balance between saturation-dependent diffusion and microbial consumption of O₂, which in turn depends on the quantity, quality and distribution of soil organic matter in the soil matrix ~~terms~~ and environmental factors like temperature and pH, which control microbial activity (Tecon and Or, 2017; Nunan, 2017; Smith et al., 2003). In fact, water films around decaying plant material may suffice to induce anaerobic respiration, if microbial respiration exceeds O₂ diffusion through that minute barrier (Parkin, 1987; Kravchenko et al., 2017).

The interplay between physical constraints and biological activity in soil controls microbial respiration at microscopic scales and complicates the prediction of denitrification and N-gas fluxes at larger scales. For instance, nitrous oxide (N₂O) emissions ~~show are~~ notoriously ~~large spatial variability~~ variable in space, which has been attributed to heterogeneous distribution of anoxic microsites in the soil (Mathieu et al., 2006; Röver et al., 1999; Parkin, 1987; Parry et al., 1999). Together with the often observed high temporal variability of microbial respiration and its fluctuations under transient conditions, this has led to the notion of “hotspots” and “hot moments” for microbial activity and emissions (Groffman et al., 2009; Kuzyakov and Blagodatskaya, 2015). “Hotspots” of denitrification have traditionally been linked to diffusion

constraints in soil aggregates (Smith, 1980; Arah and Vinten, 1995). Cell numbers and O₂ concentration have been shown to decline exponentially towards aggregate centers (Sexstone et al., 1985; Horn et al., 1994; Zausig et al., 1993; Højberg et al., 1994) and the critical aggregate
75 radius for the development of anoxic centers and is variable but typically >1 mm (Sierra and Renault, 1996; Højberg et al., 1994; Schlüter et al., 2018). However, anoxic microsites have also been reported for smaller aggregates (equivalent diameter of 0.03-0.13 mm) in well-aerated, repacked soils (Keiluweit et al., 2018).

An important, but often neglected aspect of physical diffusion constraints on microbial respiration
80 is the spatial distribution of microbial hotspots within the soil matrix. Incubation experiments were either designed to control the aggregate size in repacked soil (Mangalassery et al., 2013; Miller et al., 2009) or the volume fraction of sieved soil mixed evenly into sterile quartz sand (Keiluweit et al., 2018). Some incubation studies were carried out with undisturbed soil and investigated diffusion constraints within the pore network (Rabot et al., 2015). However, these
85 studies did not address the location-spatial distribution of hotspots nor the diffusion lengths towards air-filled pores. The vast majority of incubation studies merely reports bulk soil properties like carbon and nitrogen content, bulk density and water saturation. Notable exceptions are Kravchenko et al. (2017) who controlled the position of microbial hotspots by placing decaying plant leaf material into repacked soils with different aggregate sizes and water
90 saturations and Ebrahimi and Or (2018), who placed several layers of remolded aggregates as artificial hotspots into a sand matrix and controlled the volume fraction of anaerobic and aerobic respiration by adjusting the water table in the sand column. Such systematic studies with simplified soil aggregate analogues, yet fully accounting for transport processes from and towards hotspots, including interactions between hotspots, are needed to improve our understanding about

95 | how physical constraints on microbial respiration control the anaerobic soil volume and ~~transient~~
hence denitrification activity.

The objective of the present study was to study the interplay between microbial activity and physical diffusion in controlling aerobic and anaerobic respiration for different spatial distributions of hotspots. We embedded uniform artificial hotspots ~~inoculated~~ saturated with oxically growing ~~denitrifying~~ pure cultures (Schlüter et al., 2018) in sterile sand in two different architectures: either densely packed in two layers with minimal distance between hotspots within a layer or distributed randomly with maximum spacing between individual hotspots (Figure 1a-b), which was adjusted to different water saturations. We ~~hypothesized~~ presumed that the competition for oxygen would depend on ~~the~~ this separation distance between
105 | the hotspots, which in turn would control microbial cell growth and O₂ consumption and thus affect the timing and velocity of the aerobe-anaerobe transition in respiration, ~~i.e. the~~ with consequences for the onset of denitrification and its gaseous product stoichiometry. Further, by placing hotspots ~~inoculated~~ with complete (*P. denitrificans*) and truncated (*A. tumefaciens*) denitrifiers in distinct horizontal layers, we expected to see interactions between hotspots acting as mere N₂O sources and hotspots potentially being N₂O sinks (by reducing N₂O to N₂) with respect to overall N₂O turnover. To create contrasting velocities of oxygen transfer between headspace and hotspots, we incubated the different hotspot architectures at three water saturations thereby addressing the question how overall oxygen supply (regulated by saturation) and local oxygen availability (regulated by hotspot distribution) interact in regulating denitrification
110 | activity. The overall goal of our reductionist approach with artificial hotspots, pure bacterial strains and a closed incubation system was to reduce the inherent complexity of soil in order to (i) identify processes that governed denitrification at the pore scale and (ii) create an experimental dataset for validation of pore-scale denitrification models.
115 |

120 ~~To capture the highly dynamic respiration kinetics~~ For this, we monitored O₂, CO₂, NO, N₂O and
N₂ ~~exchange between the headspace and the sand hotspot matrix~~ at high temporal resolution and
~~The determined the~~ morphology of the air-filled pore space in terms of air connectivity, air
tortuosity and air distance ~~was determined~~ by X-ray computed tomography after the experiment.

2. Material and methods

2.1. Microbial hotspots

125 Two ~~facultative anaerobic bacteria~~ denitrifier strains were used in this study: *Paracoccus*
denitrificans expresses all denitrification enzymes necessary to reduce NO₃⁻ to N₂, whereas
Agrobacterium tumefaciens lacks the gene *nosZ* encoding nitrous oxide reductase (N₂OR), which
makes N₂O the final denitrification product. Moreover, the two strains differ in their regulatory
phenotypes with respect to inducing denitrification in response to oxygen depletion, which leads
130 to characteristic patterns of product accumulation (Bergaust et al., 2011). *P. denitrificans* induces
NO and N₂O reductase early during O₂ depletion (Bergaust et al., 2010), thus releasing little N₂O.
By contrast, *A. tumefaciens* is known to be less stringent in controlling intermediates, which may
result in the release of large amounts of NO, up to cell-toxic, milli-molar concentrations
(Bergaust et al., 2008). Both strains were grown oxically in Sistrom's medium (Sistrom, 1960) as
135 described in a previous study (Schlüter et al., 2018), but at double strength to provide enough
substrate for depleting O₂ during aerobic growth once transferred to the porous glass beads. The
medium was amended with 10 mM NH₄NO₃ and 5 mM KNO₃ for anaerobic growth. To produce
microbial hotspots, porous borosilicate glass beads (VitraPOR P100, ROBU Glasfilter Geräte
GmbH) with a diameter of 7 mm, a porosity of 32% and a medium pore diameter of 60 µm were
140 saturated with freshly inoculated growth medium (≈10⁸ cells ml⁻¹) by submersion into one of the

two cultures. In the following, the inoculated porous glass beads are referred to as *At*- (*A. tumefaciens*) and *Pd*- (*P. denitrificans*) hotspots. Detailed information about the culture conditions and the inoculation procedure can be found in Schlüter et al. (2018).

2.2. Repacked sand

145 Fifty *At* and *Pd* hotspots each were placed into 120 ml of washed, sterile quartz sand (0.2-0.5 mm grain size) yielding a volume fraction of 14% (20 ml; Fig. S1a). The sand was packed into 240 ml glass jars (Ball Corporation, Bloomfield, CA) in portions of 10 ml layers and adjusted to target saturation by adding sterile water with a spray can. The packing procedure resulted in some minor changes in porosity between layers and some larger gaps around the hotspots (Fig. S3) which affected air distribution in the sand (Fig. S2a). Three saturations were used, corresponding to water-filled pore spaces (WFPS) of 30, 60 and 90%. The fully saturated hotspots were placed into the sand at three different architectures (Fig. 1). For the “random” distribution, the hotspots were placed in five equidistant (~9.8 mm, center to center) horizontal layers with a random distribution of ten *At* and ten *Pd* hotspots per layer. The average spacing between neighboring hotspots (surface to surface) was approx. 6mm in this architecture, which was the maximum possible spacing for this amount of hotspot volume (Fig. 1b). For the “layered *At/Pd*” and “layered *Pd/At*” distributions, all fifty hotspots of each strain were placed into one of two horizontal layers spaced 21 mm from each other (center to center) at an average headspace distance of 18.2 and 39.2 mm, respectively, where the order represents *top/bottom*. The average spacing between neighboring hotspots (surface to surface) was approx. 1 mm in these densely packed layers (Fig. 1c). Care was taken to keep the hotspots cool (on crushed ice) during the packing procedure. The pore size distribution of the porous hotspots and the sand in the bulk soil and in hotspot vicinity are reported in Figure S3.

150

155

160

2.3. Incubation

165 To establish aerobic and anaerobic growth patterns and denitrification kinetics for both bacterial
strains when growing inside the porous glass beads, a pre-experiment was conducted without
sand. Fifty *Pd* or *At* hotspots were placed in empty-septum-sealed 120 ml serum bottles (Fig. S1b)
and incubated at 15°C under either oxic (He/O₂ 80/20%) or anoxic (He 100%) conditions in two
replicates per treatment. Headspace concentrations of O₂, CO₂, NO, N₂O and N₂ were measured
170 every 4 h by piercing the septum with a hypodermic needle mounted to the robotic arm of an
autosampler (GC-PAL, CTC Analytics, Switzerland). The autosampler was connected to a gas
chromatograph (Agilent Model 7890A, Santa Clara, CA, USA) and a NO analyzer (Teledyne
200. San Diego, CA, USA) via a peristaltic pump. Detailed information about the robotized
incubation system and the experimental setup can be retrieved elsewhere (Molstad et al.,
175 2007; Schlüter et al., 2018).

In the main experiment, freshly inoculated glass beads were packed into incubation vessels as
described above, three replicates for each of the nine combinations of saturation and hotspot
distribution. Jars with 30% and 60% WFPS were flushed with He/O₂ for 40 min, using ten cycles
of vacuum (3 min) and purging (1 min). Jars with 90% WFPS were flushed using 180 cycles of
180 mild vacuum (~ 600 mbar) and O₂/He purging to avoid structural changes of the packed columns
due to bubbling of trapped gas. The jars were then placed into a water bath kept at 15°C and after
temperature equilibration O₂/He overpressure was released. Gas concentrations in the headspace
were analyzed as described above. Gas production and consumption kinetics were used to
calculate the fraction of electrons diverted to O₂ or N oxyanions and thus to estimate the
185 contribution of denitrification to total respiration (e_{denit}^-/e_{total}^-) (Schlüter et al., 2018; Bergaust et
al., 2011). The NO/(NO+ N₂O + N₂) and N₂O/(NO+ N₂O + N₂) product ratios were estimated

from the cumulative release of gaseous denitrification products (NO, N₂O, N₂), after subtracting precursors from products (NO from N₂O + N₂ and NO + N₂O from N₂). The rationale behind the latter was to mimic an open system, in which N-gases released to the atmosphere are not available any longer as electron acceptors for denitrification. This approach cannot make up for the general shortcoming of closed systems that accumulate gaseous and dissolved intermediates to high concentrations, but N₂O concentrations in soil air reaching >100 ppm are reported occasionally (Risk et al., 2014; Russenes et al., 2019). Details about the calculation of denitrification product ratios can be found in the Supporting Information (SI 1.2).

2.4. X-ray tomography and image analysis

After the incubation experiment, the glass jars were scanned with X-ray micro-tomography (X-tek XCT 225, Nikon Metrology) with a beam energy of 145 kV, a beam current of 280 μA, an exposure time of 708 ms per frame, a 0.5 mm copper filter for reducing beam hardening artefacts and a total of 3000 projection for a full scan. Individual hotspots were also scanned (100 kV, 90μA, 1000ms per frame, no filter) to analyze the internal pore morphology. The 2D projections were reconstructed into a 3D image with a resolution of 35 μm using a filtered-back projection algorithm in the X-tek CT Pro 3D software. Image processing from raw gray-scale data (**Fig. 1a**) to segmented data including sand grains, air and water (**Fig. 1b-c**) was carried out according to well-established protocols for multi-phase segmentation (Schlüter et al., 2014). The porous glass beads were assigned to *At* or *Pd* hotspots according to the orientation of the flat end in the random architecture or by the vertical position in the layered architecture (**Fig. 1b-c**). The segmented images were analyzed with respect to three different spatial attributes of the air-filled pore spaces deemed important for oxygen supply. 1. Air connectivity by distinguishing isolated air-filled pores and air-filled pores with a continuous path to the headspace (yellow and red in

210 **Fig. 1d**). Air connectivity is then defined as the ratio of connected air-filled pore space and total
air-filled pore space 2. Air tortuosity as derived from the geodesic length of connected air-filled
pores. The geodesic length is the distance of any connected air voxel to the headspace along
curved paths around obstacles like solid particles and water-blocked pores (**Fig. 1e**). Air
tortuosity is the ratio between geodesic and vertical Euclidean distance to the headspace averaged
215 over all connected, air-filled voxels. It is a proxy for the diffusive transport of gaseous oxygen in
air-filled pores 3. Air distances of water-filled pores as defined by the average geodesic distance
from any water voxel to the closest air-filled pore with headspace connection (white in **Fig. 1f**).
Air distance is a proxy for the slow diffusive transport of dissolved oxygen. All image processing
steps were carried out with Fiji/ImageJ (Schindelin et al., 2012) and associated plugins (Legland
220 et al., 2016; Doube et al., 2010) or with VG Studio Max 2.1 (Volume Graphics). Each image
processing and analysis step is explained in detail in the supporting information (**SI 1.3**).

[Figure 1]

3. Results

3.1. Aerobic respiration and denitrification in unconstrained

225 hotspots without sand

At grew faster than *Pd* at 15°C in the experiment with loosely placed porous glass beads as
indicated by faster O₂ consumption and CO₂ accumulation in the oxic treatment (**Figure 2a,b**).
Also under fully anoxic conditions, *At* accumulated CO₂ faster than *Pd* (Figure 2b). N-gas
kinetics clearly reflected the ~~distinct-disparate~~ regulatory phenotypes of the two bacterial
230 denitrifiers. Anoxic *At* instantly accumulated a large amounts of NO (**Figure 2c**) which persisted
until all NO₃⁻ was reduced to N₂O (as judged from the stable plateau in N₂O, **Figure 2d**). Due to

slower growth and O₂ consumption, *Pd* induced denitrification much later than *At*, but accumulated less intermediates (NO, N₂O) than *At*. Oxically incubated *Pd* accumulated no detectable NO, indicating efficient regulation of denitrification when switched slowly to anaerobic conditions in hotspots. Also, NO may have been reduced to N₂O when diffusing from the anoxic center to the boundary of the hotspots. In the initially oxically treatments, denitrification contributed 7% to the total electron flow in *At* hotspots and 13% in *Pd* hotspots measured over the entire period, reflecting the fact that (i) *Pd* has one more reduction step in the denitrification sequence and that (ii) *At* used less nitrate for anaerobic respiration in anoxic hotspots centers and more oxygen for aerobic respiration in oxically hotspots margins than *Pd*.

[Figure 2]

3.2. Effects of hotspot distribution in sand

The distribution of microbial hotspots within the sand strongly impacted bulk respiration. This is evident for treatments with medium saturation (60% WFPS) for the first 210 h of incubation (**Figure 3**) and with other saturations for the entire incubation period (300 h; **Figures S4-6**). The random distribution of hotspots allowed for much faster aerobic growth than the layered architectures, leading to complete consumption of O₂ from the jars after-within 70 h (**Figure 3a**). Given the slow growth of *Pd* (**Figure 2a**), initial O₂ consumption was dominated by the activity of *At* hotspots turning them partly anoxic. Hence, the pronounced NO peak in the random treatment, coinciding with complete O₂ exhaustion from the headspace (**Figure 3c**), was due to *At* activitydenitrification, similar to what was seen in the unconstrained *At* hotspots under anoxic conditions (**Figure 2c**). N₂O production was observed long before O₂ was depleted from the headspace (**Figure 3d**) and is attributed entirely to *At* denitrification. *Pd* denitrification did not start before all O₂ was depleted and manifested itself in a transient increase in N₂O production at

255 ~70 h together with an exponential increase in N₂ production (**Figure 3e**) which was also observed with unconstrained *Pd* hotspots (**Figure 2e**). Note that the apparent net consumption of CO₂ (**Figure 3b**) upon O₂ depletion was due to internal alkalization driven by accelerating denitrification, once all hotspots turned anoxic.

[Figure 3]

260 In the layered architectures, O₂ consumption was slower and complete anoxia was not reached before 120 h into the incubation. In contrast to the random architecture, less O₂ was available for each individual hotspot in the densely packed hotspot layers, allowing for less aerobic growth per unit time. As a consequence, there was more time for fully denitrifying *At* hotspots to interact with *Pd* hotspots which induced denitrification gradually between 80 and 120 h. Indeed, less N₂O
265 accumulated in the headspace than in the random treatment (**Figure 3d, S6d**) and the onset of N₂ accumulation appeared long before complete O₂ depletion ~~from-in~~ the headspace (**Figure 3a,e**). In other words, *Pd* hotspots consumed N₂O produced in *At* hotspots. Upon O₂ depletion in the headspace, a burst of NO production occurred (**Figure 3c**) as seen previously with *At* hotspots (**Figure 2c**). However, since *Pd* denitrification was now fully developed, the NO peak was much
270 more short-lived than with the random distribution, because *Pd* hotspots reduced NO produced by *At* hotspots all the way to N₂.

The effect of vertical order in the layered hotspot architecture was small, but consistent among all denitrification products. The distribution with *Pd* hotspots on top (layered *Pd/At*) consumed the NO and N₂O produced in *At* hotspots much quicker than the *At/Pd* architecture (**Figure 3c-d**) and
275 accumulated N₂ faster after complete O₂ depletion (**Figure 3e**). Both observations highlight the effect of shorter diffusion distances between the headspace and the *Pd* hotspot layer in the layered *Pd/At* architecture.

3.3. Effects of matrix saturation

Differences in water saturation resulted in different absolute amounts of oxygen initially present
280 in the jars (**Figure 4a**) but did not affect the O₂ concentration in the sand matrix. Oxygen was
depleted slightly faster at 60% than at 90% saturation even though there was absolutely more O₂
initially present at 60% WFPS. This illustrates the paramount role of oxic growth for the oxic-
anoxic transition in the hotspots: the more O₂ available initially, the stronger the aerobic growth
and the faster the oxic-anoxic transition.

285 Increasing saturation from 60 to 90% in the randomly distributed hotspots had a strong effect on
the timing and accumulation of denitrification products. The expected NO burst upon O₂
depletion was damped by two orders of magnitude (**Figure 4c**), because the oxic-anoxic
transition proceeded more smoothly in the 90% treatment and NO was reduced further to N₂O
before it could escape to the headspace. On the other hand, N₂O and N₂ production commenced
290 earlier in the 90% than in the 60% treatment (**Figure 4d-e**), indicating that O₂ availability was *a*
priori smaller irrespective of metabolic activity (which was larger in the 60% treatment). The
switch from net N₂O production to net N₂O consumption indicates the moment when microbial
activity in *Pd* hotspots caught up with *At* hotspots.

[Figure 4]

295 Surprisingly, O₂ consumption in the 30% treatments was slow despite having the largest amount
of O₂ in the jar. This was caused by unintended substrate limitation. Due to overlapping pore size
distribution between porous hotspots and sand (**Fig. S3c**), medium was sucked by capillary force
from the hotspot into the surrounding sand, as could be seen in a parallel experiment with brilliant
blue dye (**Fig. S7**). This separated bacterial cells, which were likely immobilized in the pore
300 space of the hotspots, temporarily from a considerable fraction of the carbon and NO₃⁻ supplied

with the medium, before the dissolved substrate would diffuse back into the hotspots due to the evolving gradient induced by consumption in the hotspots. Decreasing the saturation from 60% to 30% also resulted in different timing and accumulation of denitrification products. The slow oxic growth of both *At* and *Pd* hotspots due to the substrate diffusion limitation at 30% WFPS provided more time for *Pd* hotspots to interact with *At* hotspots than in the 60% WFPS treatment. Indeed, the NO burst from *At* hotspots after complete O₂ exhaustion in the random architecture was 50% higher at 30% WFPS indicating higher *At* cell numbers due to prolonged oxic growth (Figure 4c, ~~Figure 5e~~), whereas the N₂O peak was 50% lower, due to concomitant N₂O reduction in *Pt* hotspots (Figure 4d, ~~Figure 5d~~).

310 3.4. Mass balances

By the end of the incubation, oxygen was exhausted in all treatments. Likewise, NO₃⁻ was consumed by all treatments, except for the layered hotspots at 30% and 60% WFPS. This means that respiration was electron acceptor limited and that the cumulated recovery of denitrification products can be compared with the amount of NO₃⁻ initially present (Figure S8). The balance between aerobic and anaerobic respiration, e_{denit}^-/e_{total}^- (Bergau et al., 2011), is given by the electron flow to nitrogenous electron acceptors relative to the total electron flow, including O₂ respiration (Figure 5). When seen over all three water saturations, early stage denitrification under oxic headspace conditions (Figure 5a) showed a threshold response to increasing moisture with disproportionally higher e_{denit}^-/e_{total}^- ratios at 90% WFPS (17-27%) than at 60% or 30%. The proportions of electrons diverted to denitrification at low and medium saturations were small (2-7%) and even smaller than those observed in unconstrained hotspots (7-13%). Differences between saturations were less pronounced when the entire incubation period is considered (Figure 5b), since fully anoxic conditions during late stage incubation overrode saturation

325 | effects. Overall, the effect of hotspot architecture on e_{denit}^-/e_{total}^- ratios was smaller than the effect of saturation.

This stands in stark contrast to the pronounced effect of hotspot architecture on denitrification product ratios (**Figure 5c, d**). Hotspot architecture governed growth rates through local competition for O₂ and therewith the number of active cells involved in net production sites (*At* hotspots) and net consumption sites (*Pd* hotspots) of NO once O₂ was exhausted. In layered hotspots there was hardly any net-release of NO to the headspace irrespective of saturation (**Figure 5c**). With random hotspot architecture, there was substantial NO release, the magnitude of which, however, decreased linearly with saturation. This pattern in NO stoichiometry clearly reflects the number of *At* cells at the moment of complete O₂ depletion, as affected by oxic growth which lasted longer with lower saturation. The N₂O product ratio (**Figure 5d**) was influenced by both saturation and hotspot architecture. In layered architectures, the N₂O ratio increased exponentially with increasing saturation similar to what was observed for relative electron flow to denitrification (**Figure 5a**). In random architectures, the N₂O product ratio was consistently higher than in layered architectures irrespective of saturation, yet the highest ratio was reached at 60% WFPS, due to the most vigorous growth, and hence fastest oxic-anoxic transition at intermediate saturation.

[Figure 5]

3.5. Pore space properties

At the lowest saturation (30% WFPS), the entire air-filled pore space was connected to the headspace (**Figure 6a**) and tortuosity was close to unity, i.e. the diffusion lengths in air only depended on the vertical distance to the headspace (**Figure 6b**). The diffusion distances in water-

filled pores (**Figure 6c**) corresponded to the size of small, evenly distributed water clusters. At medium saturation (60% WFPS), the amount of disconnected air was still negligible and tortuosity only slightly increased. The increase in air distance was due to a few large water pockets, which were caused by the step-wise addition of water to the repacked sand. Only at 90% saturation a considerable air volume of 5-20% became disconnected from the headspace. The path along which the remaining air was connected to the headspace became more tortuous with increasing saturation and average diffusion distances in water to the connected air cluster increased to 1 mm. This is still surprisingly short as compared to the size of the hotspots (7 mm). Independent tests showed that the high air connectivity at this low air content was facilitated by vacuum application during He/O₂-purging prior to the incubation. Directly after packing, the continuous air cluster only reached 10-15 mm into the sand (data not shown), whereas bubbling due to vacuum application formed continuous air channels that reached deep into the sand matrix connecting even the deepest hotspots with the headspace. Moreover, some larger gaps remained around hotspots during packing which tended to be air-filled after wetting. This is reflected in the consistently higher air-connectivity, lower air tortuosity and lower air distance, when only pores in the direct vicinity of hotspots are analyzed (**Figure 6a-c**). More than 90% of hotspot surfaces still had a direct air-filled connection with the headspace at 90% WFPS (**Figure 6a**). Depth profiles of these pore space attributes are reported in **Fig. S2**.

[Figure 6]

365 4. Discussion

4.1. Physical constraints on denitrification kinetics

The experimental setup in this incubation study was designed to investigate physical constraints on microbial respiration in hotspots as affected by the interplay between gaseous diffusion through a sterile matrix and local competition for oxygen. For this, we compared different combinations of water saturation in the matrix and spatial distributions of hotspots, which led to different physical constraints for the supply of hotspots with oxygen. As a consequence, oxic growth rates differed among treatments which had various implications on denitrification as summarized in a conceptual scheme (Figure 7).

[Figure 7]

375 ~~The Our~~ setup is a coarse simplification of soil in which metabolic activity in hotspots not only depends on oxygen supply, but also on diffusion of substrates from the matrix to the hotspots. As such, our experiment does not allow to draw direct conclusions about the functioning of hotspots in real soils ~~with respect to denitrification and its product stoichiometry~~. However, by placing denitrifiers and their substrates into hotspots, we considerably reduced the level of complexity and created a system that is amenable to studying the dynamic interrelations between denitrifier growth, oxygen consumption and induction of denitrification by gas kinetics.

380
385 Soil N₂O emissions are known to be highly variable in time and a unifying concept incorporating dynamic changes in denitrification activity and product stoichiometry in response to changing environmental conditions is still missing. Our model system provides a first data set for validating mathematical process models that are explicit for structural distribution of hotspots and dynamic changes in boundary conditions (here mimicked by different hotspot architectures and

declining oxygen concentrations in the headspace ~~of~~during batch incubations, respectively). The development of such models is a core activity of the DASIM project (<http://www.dasim.net/>). By combining metabolic measurements with advanced structural imaging and computation, we also
390 provide a link to parameterizing such models with real soil data in future research.

Inoculating growing denitrifiers into porous glass beads and embedding them in sterile sand resulted in a highly dynamic system with respect to oxygen consumption and induction of denitrification. This was intended for the sake of experimental depth, but it must be noted that oxic-anoxic transitions are likely slower, i.e. less dynamic in real-soil hotspots. In real soils, even
395 highly organic hotspots contain a fair amount of recalcitrant organic C that limits microbial growth and oxygen consumption. Also with respect to denitrification stoichiometry, real soils may be expected to be less dynamic as multiple denitrifying phenotypes contained in the natural soil microbiome (Roco et al., 2017) utilize denitrification intermediates mutually. Notwithstanding, soil NO and N₂O emissions are known to be episodic in nature. Large,
400 denitrification driven emission pulses occur upon abrupt changes in O₂ availability, caused by external factors like heavy rainfalls or soil freezing (Flessa et al., 1995), O₂ consumption by nitrification after ammoniacal fertilization (Huang et al., 2014) or incorporation of easily degradable organic matter (Flessa et al., 1995) which cannot be captured satisfactorily by common steady-state models for soil respiration and N₂O emission (Parton et al., 2001;Li et al.,
405 1992). Even though the concept of hotspots is central in the understanding of denitrification dynamics in upland soils, common soil denitrification models do not account for the dynamics of spatially explicit hotspots in the soil matrix but rather scale bulk denitrification with a generic anoxic volume fraction (Li et al., 2000;Blagodatsky et al., 2011). To advance soil denitrification models, it is obvious that microbial respiration dynamics in hotspots have to be targeted, both

410 conceptually (Wang et al., 2019) and experimentally (Kravchenko et al., 2017; Ebrahimi and Or, 2018). Our study is a first step in this direction.

One of the main findings of this study is that soil microbial respiration and the propensity to develop denitrifying anoxic hotspots does depend on their distribution in space. The onset of denitrification and its kinetics ~~was~~ were linked to the spatial and temporal extent of anoxia
415 developing in hotspot centers, which was governed by the interplay between denitrifier growth, ~~and~~ diffusional constraints and hotspot architecture ~~had a strong impact on this interplay~~. When distributed randomly, microbial activity was most disperse relative to available oxygen, resulting in more growth, faster O₂ draw down and earlier anoxia than when packed densely in layers (**Figure 3**). Rapid oxic-anoxic transition led to higher release rates of denitrification intermediates
420 ~~and~~ increasing the product ratios of NO and N₂O product ratios (**Figure 5c-d**). This effect was most pronounced at low and intermediate saturations but was dampened at 90% WPFS because oxygen supply was impeded by bulk diffusion irrespective of hotspot placement. Thus, our results highlight the significance of hotspot distribution at low soil moistures and exemplifies why N₂O emissions are notoriously difficult to predict under these conditions.

425 Even though we failed to fully synchronize *At* and *Pd* growth in time, our experiment demonstrates that contrasting denitrification phenotypes may interact in modulating N₂O flux to the atmosphere. *Pd* hotspots reduced N₂O released from *At* hotspots irrespective of the layers' orientation (**Figure 3d**), which can be attributed to the high degree of air connectivity in the sand column (**Figure 1d**). We had expected more N₂O reduction with *Pd* on top (layered *Pd/At*), but
430 since *At* grew faster than *Pd*, partial anoxia and NO and N₂O formation was induced in *At*, long before N₂O consuming activity was induced in *Pd* hotspots. Future experiments with artificial

hotspots should therefore carefully consider potential growth rates and air connectivity in packed soil.

4.2. Physical constraints on cumulative denitrification

435 The cumulative release of gaseous denitrification products, as described by electron flow ratios, depended less on hotspot architecture than on soil moisture. Electron flows to denitrification ranged from <5% of total respiratory flow at low to medium saturations (30, 60% WFPS) to almost 23% at 90% WFPS (**Figure 5a**). We attribute the generally is-low denitrification electron flow in our experiments to the small active volume relative to the sterile sand matrix (the total
440 volume fraction of hotspots was 14%, less of which was actually anoxic) and the large amount of oxygen initially present in the incubation jars. Yet, we found a typical, non-linear denitrification response to soil moisture (**Figure 5a**). This threshold behavior is well known (Weier et al., 1993) and has been attributed to a disproportional contribution of small pores to the anoxic volume at higher saturation (Schurgers et al., 2006). In our system, consisting of coarse sand with a
445 relatively homogenous pore size distribution, we attribute the non-linear response to an increase in tortuosity of air-filled pores and an increase in distance to the next continuous air-filled pore that weres pronounced enough to impair the oxygen supply of to hotspots with oxygen. Air connectivity and distance to the next continuous, air filled pore also increased non-linearly, but did not reach a critical value (**Figure 6**), ruling out that differences in NO and N₂O release at
450 different saturations were due to gas entrapment but rather due to elongated diffusion pathways in air-filled and water-filled pores networks, leading to longer residence times of denitrification intermediates and stronger reduction of intermediates in hotspots along the way to the headspace.

We cannot rule out bacterial spread out of the hotspots and that some denitrification might have occurred in the sand matrix. Nitrate and dissolved carbon diffused out of the hotspots and in

455 addition at the lowest saturation (30%WFPS) those substrates were transported convectively by
capillary forces. This was demonstrated with a separate dye experiment (Figure S7). The fact that
oxygen consumption was slow at 30%WFPS is indirect evidence that most bacteria remained in
the hotspots. In other words, under well-aerated conditions only substrate limitation can explain a
460 reduction in microbial growth as compared to the 60%WFPS and this can only occur if the
substrates left the hotspots, but the cells did not follow to the same degree. For the 60% and
90%WFPS cases it is unclear as to how bacterial dispersal is really relevant. *A. tumefaciens* is
known to possess flagella (Merritt et al., 2007), but *P. denitrificans* is not motile. Experimental
data on bacterial dispersal rates in soil is scarce. In a recent study with *Bacillus subtilis* and
465 *Pseudomonas fluorescens* inoculated to repacked soils at similar bulk density (1.5g/cm³) and
saturation (60%) the first cells appeared in a distance of 15mm after nine days (Juyal et al., 2018).
In our experiment, with the highest substrate concentration and the largest internal surface area in
the hotspots denitrification occurred after 3-6 days. Hence, some cells may have colonized the
immediate vicinity of hotspots, but cell densities outside the hotspots were likely low.

Saturation-dependent threshold behavior for denitrification is a well-studied phenomenon in soils
470 (Linn and Doran, 1984;Ruser et al., 2006;Paul et al., 2003), but for a lack of pore scale
measurements often attributed to reduced bulk soil diffusivity. In undisturbed soil, the relative
importance of air connectivity and distances between air-filled and water-filled pores might be
more relevant for impairing oxygen supply and inducing denitrification. Air connectivity to the
headspace was shown to affect N₂O emissions in terms of ~~intensity and speed~~magnitude and
475 responsiveness in repeated wetting/drying cycles in an intact soil column (Rabot et al., 2015). In
agricultural soil with different crop rotations, N₂O emissions were shown to correlate positively
with the volume fraction of soil with macropore distances larger than 180 μm, which was used as
an *ad-hoc* definition for poorly aerated soil (Kravchenko et al., 2018). In a mesocosm study on

microstructural drivers for local redox conditions, none of the investigated soil pore metrics
480 derived from X-ray CT data (excluding those examined here) correlated with redox kinetics
during a wetting/drying cycle (Wanzek et al., 2018). Hence, combining metabolic monitoring by
high-resolution gas kinetics with direct assessment of diffusion lengths of gaseous and dissolved
oxygen and denitrification products via X-ray microtomography emerges as a promising tool to
study physical constraints for aerobic and anaerobic respiration in soil. However, meaningful
485 metrics derived from X-ray data relevant for denitrification are yet to be developed and will
require additional experiments with both artificial and real soils. Improved understanding of
factors and mechanisms controlling denitrification and N gas emission on a three-dimensional
micro-scale may help to design and test soil management strategies that mediate the return of
excess nitrogen to the atmosphere in a controlled way, i.e. with as little as possible NO and N₂O
490 release, be it by crop residue (Kravchenko et al., 2017), pH (Russenet et al., 2016) or irrigation
(Bergstermann et al., 2011) management. At the same time, our experiments call for the
implementation of spatially explicit reaction-diffusion algorithms (Hron et al., 2015;Ebrahimi and
Or, 2016) in soil process models. For instance, diffusion lengths between hotspots and air-filled
pores connected to the headspace may serve as a useful ~~measure-metric~~ to ~~parametrize-be~~
495 implemented on model concepts like the anaerobic soil volume fraction in larger-scale continuum
models (Li et al., 2000;Schurgers et al., 2006;Blagodatsky et al., 2011).

5. Conclusions

Using a highly simplified model system, we demonstrate that the denitrification in heterogeneous
media like soil ~~factorial combination of~~critically depends on water saturation and-as well as on
500 the spatial distribution of microbial ~~hotspots-architecture~~ creates a wealth of denitrification
kinetics in response to declining oxygen concentrations with highly variable. Hotspot architecture

effects were particularly pronounced with respect to denitrification stoichiometry resulting in vastly different NO and N₂O release rates. Even though our experiment was conducted in a closed system, with growing denitrifier strains and a limited amount of substrate, the results are relevant for real soils in that they ~~give a worst-case~~ represent a bench-mark scenario of ~~population dynamics and metabolic activity in hotspots~~ hotspot-driven denitrification. More importantly, our reductionist approach resulted in an experimental dataset that is amenable to process-based, pore-scale denitrification models, which will be the subject of a future study.

Hotspot architecture played a more pronounced role for denitrification kinetics at lower soil moisture (30 and 60% WFPS). Hence, denitrification and its gaseous product stoichiometry do not only depend on the amount of microbial hotspots in aerated soil, but also on their spatial distribution. The total amount of denitrification measured as cumulative electron flow, in turn, depended more on water saturation which is in line with the well-known saturation-dependent threshold behavior in denitrification also found in natural soil. For the case of artificial soil used in our study, we found that this threshold behavior was best explained by increased air tortuosity and air distance at high saturations. Future experiments with artificial and natural soils are needed to fully capture the regulation of denitrification at the micro-scale.

6. Data availability

All segmented X-ray μ CT files and the GC data are permanently available through the UFZ archive with data description using standardized metadata catalogue (Dublin Core) and with access via URL: <http://www.ufz.de/record/<to-be-filled-after-acceptance>>.

7. Author contribution

SS, HV and PD designed the experiments. SS, JZ and PD carried them out. SS, JZ and PD processed the data. SS prepared the manuscript with contributions from all co-authors.

525

8. Competing interests

The authors declare that they have no conflict of interest.

6.9. Acknowledgments

We thank Ali Ebrahimi and an anonymous reviewer for the constructive comments. This study was funded by the Deutsche Forschungsgemeinschaft through the research unit DFG-FOR 2337: Denitrification in Agricultural Soils: Integrated Control and Modelling at Various Scales (DASIM). PD received funding from the FACCE-ERA-GAS project MAGGE-pH under the Grant Agreement No. 696356. We thank Linda Bergaust for providing the bacterial strains, Jing Zhu for laboratory support and Olaf Ippisch and Marcus Horn for helpful discussions during the planning of the experiment.

535

7.10. References

536 Arah, J. R. M., and Vinten, A. J. A.: Simplified models of anoxia and denitrification in
537 aggregated and simple-structured soils, *European Journal of Soil Science*, 46, 507-517, DOI
538 10.1111/j.1365-2389.1995.tb01347.x, 1995.

539 Ball, B. C.: Soil structure and greenhouse gas emissions: a synthesis of 20 years of
540 experimentation, *European Journal of Soil Science*, 64, 357-373, 10.1111/ejss.12013, 2013.

541 Bergaust, L., Shapleigh, J., Frostegard, A., and Bakken, L.: Transcription and activities of NOx
542 reductases in *Agrobacterium tumefaciens* : The influence of nitrate, nitrite and oxygen
543 availability, *Environ. Microbiol.*, 10, 3070-3081, 2008.

544 Bergaust, L., Mao, Y., Bakken, L., and Frostegard, A.: Denitrification response patterns during
545 the transition to anoxic respiration and posttranscriptional effects of suboptimal pH on nitrogen
546 oxide reductase in *Paracoccus denitrificans* *Appl. Environ. Microbiol.*, 76, 6387-6396, 2010.

547 Bergaust, L., Bakken, Lars R., and Frostegård, A.: Denitrification regulatory phenotype, a new
548 term for the characterization of denitrifying bacteria, *Biochemical Society Transactions*, 39, 207-
549 212, 10.1042/bst0390207, 2011.

550 Bergstermann, A., Cárdenas, L., Bol, R., Gilliam, L., Goulding, K., Meijide, A., Scholefield, D.,
551 Vallejo, A., and Well, R.: Effect of antecedent soil moisture conditions on emissions and
552 isotopologue distribution of N₂O during denitrification, *Soil Biology and Biochemistry*, 43, 240-
553 250, <https://doi.org/10.1016/j.soilbio.2010.10.003>, 2011.

554 Blagodatsky, S., Grote, R., Kiese, R., Werner, C., and Butterbach-Bahl, K.: Modelling of
555 microbial carbon and nitrogen turnover in soil with special emphasis on N-trace gases emission,
556 *Plant and Soil*, 346, 297, 10.1007/s11104-011-0821-z, 2011.

557 Doube, M., Kłosowski, M. M., Arganda-Carreras, I., Cordelières, F. P., Dougherty, R. P.,
558 Jackson, J. S., Schmid, B., Hutchinson, J. R., and Shefelbine, S. J.: BoneJ: Free and extensible
559 bone image analysis in *ImageJ*, *Bone*, 47, 1076-1079, 2010.

560 Ebrahimi, A., and Or, D.: Microbial community dynamics in soil aggregates shape
561 biogeochemical gas fluxes from soil profiles - upscaling an aggregate biophysical model, *Global
562 Change Biology*, 22, 3141-3156, 2016.

563 Ebrahimi, A., and Or, D.: Dynamics of soil biogeochemical gas emissions shaped by remolded
564 aggregate sizes and carbon configurations under hydration cycles, *Global Change Biology*, 24,
565 e378-e392, 10.1111/gcb.13938, 2018.

566 Elberling, B., Askaer, L., Jørgensen, C. J., Joensen, H. P., Kühl, M., Glud, R. N., and Lauritsen,
567 F. R.: Linking Soil O₂, CO₂, and CH₄ Concentrations in a Wetland Soil: Implications for CO₂
568 and CH₄ Fluxes, *Environmental Science & Technology*, 45, 3393-3399, 10.1021/es103540k,
569 2011.

570 Flessa, H., Dörsch, P., and Beese, F.: Seasonal variation of N₂O and CH₄ fluxes in differently
571 managed arable soils in southern Germany, *Journal of Geophysical Research: Atmospheres*, 100,
572 23115-23124, doi:10.1029/95JD02270, 1995.

573 Groffman, P. M., Butterbach-Bahl, K., Fulweiler, R. W., Gold, A. J., Morse, J. L., Stander, E. K.,
574 Tague, C., Tonitto, C., and Vidon, P.: Challenges to incorporating spatially and temporally
575 explicit phenomena (hotspots and hot moments) in denitrification models, *Biogeochemistry*, 93,
576 49-77, 2009.

577 Højberg, O., Revsbech, N. P., and Tiedje, J. M.: Denitrification in soil aggregates analyzed with
578 microensors for nitrous oxide and oxygen, *Soil Science Society of America Journal*, 58, 1691-
579 1698, 1994.

580 Horn, R., Stepniewski, W., Włodarczyk, T., Walenzik, G., and Eckhardt, F.: Denitrification rate
581 and microbial distribution within homogeneous model soil aggregates, *Int. Agrophysics*, 8, 65-
582 74, 1994.

583 Hron, P., Jost, D., Bastian, P., Gallert, C., Winter, J., and Ippisch, O.: Application of Reactive
584 Transport Modeling to Growth and Transport of Microorganisms in the Capillary Fringe, *Vadose*
585 *Zone Journal*, 14, 10.2136/vzj2014.07.0092, 2015.

586 Huang, T., Gao, B., Hu, X.-K., Lu, X., Well, R., Christie, P., Bakken, L. R., and Ju, X.-T.:
587 Ammonia-oxidation as an engine to generate nitrous oxide in an intensively managed calcareous
588 Fluvo-aquic soil, *Scientific Reports*, 4, 3950, 10.1038/srep03950

589 <https://www.nature.com/articles/srep03950#supplementary-information>, 2014.

590 Juyal, A., Eickhorst, T., Falconer, R., Baveye, P. C., Spiers, A., and Otten, W.: Control of Pore
591 Geometry in Soil Microcosms and Its Effect on the Growth and Spread of *Pseudomonas* and
592 *Bacillus* sp, *Frontiers in Environmental Science*, 6, 10.3389/fenvs.2018.00073, 2018.

593 Keiluweit, M., Wanzek, T., Kleber, M., Nico, P., and Fendorf, S.: Anaerobic microsites have an
594 unaccounted role in soil carbon stabilization, *Nature Communications*, 8, 1771, 10.1038/s41467-
595 017-01406-6, 2017.

596 Keiluweit, M., Gee, K., Denney, A., and Fendorf, S.: Anoxic microsites in upland soils
597 dominantly controlled by clay content, *Soil Biology and Biochemistry*, 118, 42-50,
598 <https://doi.org/10.1016/j.soilbio.2017.12.002>, 2018.

599 Kravchenko, A. N., Toosi, E. R., Guber, A. K., Ostrom, N. E., Yu, J., Azeem, K., Rivers, M. L.,
600 and Robertson, G. P.: Hotspots of soil N₂O emission enhanced through water absorption by plant
601 residue, *Nature Geoscience*, 10, 496, 10.1038/ngeo2963

602 <https://www.nature.com/articles/ngeo2963#supplementary-information>, 2017.

603 Kravchenko, A. N., Guber, A. K., Quigley, M. Y., Koestel, J., Gandhi, H., and Ostrom, N. E.: X-
604 ray computed tomography to predict soil N₂O production via bacterial denitrification and N₂O
605 emission in contrasting bioenergy cropping systems, *GCB Bioenergy*, 0,
606 doi:10.1111/gcbb.12552, 2018.

607 Kuzyakov, Y., and Blagodatskaya, E.: Microbial hotspots and hot moments in soil: Concept &
608 review, *Soil Biology and Biochemistry*, 83, 184-199, 2015.

609 Legland, D., Arganda-Carreras, I., and Andrey, P.: MorphoLibJ: integrated library and plugins
610 for mathematical morphology with ImageJ, *Bioinformatics*, 32, 3532-3534, 2016.

611 Li, C., Frolking, S., and Frolking, T. A.: A model of nitrous oxide evolution from soil driven by
612 rainfall events: 1. Model structure and sensitivity, *Journal of Geophysical Research:*
613 *Atmospheres*, 97, 9759-9776, doi:10.1029/92JD00509, 1992.

614 Li, C., Aber, J., Stange, F., Butterbach-Bahl, K., and Papen, H.: A process-oriented model of
615 N₂O and NO emissions from forest soils: 1. Model development, *Journal of Geophysical*
616 *Research: Atmospheres*, 105, 4369-4384, 2000.

617 Linn, D., and Doran, J.: Effect of water-filled pore space on carbon dioxide and nitrous oxide
618 production in tilled and nontilled soils, *Soil Science Society of America Journal*, 48, 1267-1272,
619 1984.

620 Mangalassery, S., Sjögersten, S., Sparkes, D. L., Sturrock, C. J., and Mooney, S. J.: The effect of
621 soil aggregate size on pore structure and its consequence on emission of greenhouse gases, *Soil*
622 *and Tillage Research*, 132, 39-46, <https://doi.org/10.1016/j.still.2013.05.003>, 2013.

623 Mathieu, O., Lévêque, J., Hénault, C., Milloux, M.-J., Bizouard, F., and Andreux, F.: Emissions
624 and spatial variability of N₂O, N₂ and nitrous oxide mole fraction at the field scale, revealed with
625 ¹⁵N isotopic techniques, *Soil Biology and Biochemistry*, 38, 941-951, 2006.

626 Merritt, P. M., Danhorn, T., and Fuqua, C.: Motility and chemotaxis in *Agrobacterium*
627 *tumefaciens* surface attachment and biofilm formation, *J Bacteriol*, 189, 8005-8014,
628 10.1128/JB.00566-07, 2007.

629 Miller, M. N., Zebarth, B. J., Dandie, C. E., Burton, D. L., Goyer, C., and Trevors, J. T.:
630 Denitrifier Community Dynamics in Soil Aggregates under Permanent Grassland and Arable
631 Cropping Systems, *Soil Science Society of America Journal*, 73, 1843-1851,
632 10.2136/sssaj2008.0357, 2009.

633 Molstad, L., Dörsch, P., and Bakken, L. R.: Robotized incubation system for monitoring gases
634 (O₂, NO, N₂O, N₂) in denitrifying cultures, *Journal of Microbiological Methods*, 71, 202-211,
635 2007.

636 Moyano, F. E., Vasilyeva, N., Bouckaert, L., Cook, F., Craine, J., Curiel Yuste, J., Don, A.,
637 Epron, D., Formanek, P., Franzluebbers, A., Ilstedt, U., Kätterer, T., Orchard, V., Reichstein, M.,
638 Rey, A., Ruamps, L., Subke, J. A., Thomsen, I. K., and Chenu, C.: The moisture response of soil
639 heterotrophic respiration: interaction with soil properties, *Biogeosciences*, 9, 1173-1182,
640 10.5194/bg-9-1173-2012, 2012.

641 Nunan, N.: The microbial habitat in soil: Scale, heterogeneity and functional consequences,
642 *Journal of Plant Nutrition and Soil Science*, 180, 425-429, 10.1002/jpln.201700184, 2017.

643 Parkin, T. B.: Soil microsites as a source of denitrification variability, *Soil Science Society of
644 America Journal*, 51, 1194-1199, 1987.

645 Parry, S., Renault, P., Chenu, C., and Lensi, R.: Denitrification in pasture and cropped soil clods
646 as affected by pore space structure, *Soil Biology and Biochemistry*, 31, 493-501,
647 [https://doi.org/10.1016/S0038-0717\(98\)00101-1](https://doi.org/10.1016/S0038-0717(98)00101-1), 1999.

648 Parton, W. J., Holland, E. A., Del Grosso, S. J., Hartman, M. D., Martin, R. E., Mosier, A. R.,
649 Ojima, D. S., and Schimel, D. S.: Generalized model for NO_x and N₂O emissions from soils,
650 *Journal of Geophysical Research: Atmospheres*, 106, 17403-17419, doi:10.1029/2001JD900101,
651 2001.

652 Paul, K. I., Polglase, P. J., O'Connell, A. M., Carlyle, J. C., Smethurst, P. J., and Khanna, P. K.:
653 Defining the relation between soil water content and net nitrogen mineralization, *European
654 Journal of Soil Science*, 54, 39-48, doi:10.1046/j.1365-2389.2003.00502.x, 2003.

655 Rabot, E., Lacoste, M., Hénault, C., and Cousin, I.: Using X-ray Computed Tomography to
656 Describe the Dynamics of Nitrous Oxide Emissions during Soil Drying, *Vadose Zone Journal*,
657 14, 10.2136/vzj2014.12.0177, 2015.

658 Risk, N., Wagner-Riddle, C., Furon, A., Warland, J., and Blodau, C.: Comparison of
659 Simultaneous Soil Profile N₂O Concentration and Surface N₂O Flux Measurements Overwinter
660 and at Spring Thaw in an Agricultural Soil, *Soil Science Society of America Journal*, 78, 180-
661 193, 10.2136/sssaj2013.06.0221, 2014.

662 Roco, C. A., Bergaust, L. L., Bakken, L. R., Yavitt, J. B., and Shapleigh, J. P.: Modularity of
663 nitrogen-oxide reducing soil bacteria: linking phenotype to genotype, *Environmental
664 Microbiology*, 19, 2507-2519, doi:10.1111/1462-2920.13250, 2017.

665 Röver, M., Heinemeyer, O., Munch, J. C., and Kaiser, E.-A.: Spatial heterogeneity within the
666 plough layer: high variability of N₂O emission rates, *Soil Biology and Biochemistry*, 31, 167-
667 173, 1999.

668 Ruser, R., Flessa, H., Russow, R., Schmidt, G., Buegger, F., and Munch, J. C.: Emission of N₂O,
669 N₂ and CO₂ from soil fertilized with nitrate: effect of compaction, soil moisture and rewetting,
670 *Soil Biology and Biochemistry*, 38, 263-274, <https://doi.org/10.1016/j.soilbio.2005.05.005>, 2006.

671 Russenes, A. L., Korsæth, A., Bakken, L. R., and Dörsch, P.: Spatial variation in soil pH controls
672 off-season N₂O emission in an agricultural soil, *Soil Biology and Biochemistry*, 99, 36-46,
673 <https://doi.org/10.1016/j.soilbio.2016.04.019>, 2016.

674 Russenes, A. L., Korsæth, A., Bakken, L. R., and Dörsch, P.: Effects of nitrogen split application
675 on seasonal N₂O emissions in southeast Norway, *Nutrient Cycling in Agroecosystems*,
676 10.1007/s10705-019-10009-0, 2019.

677 Schaufler, G., Kitzler, B., Schindlbacher, A., Skiba, U., Sutton, M. A., and Zechmeister-
678 Boltenstern, S.: Greenhouse gas emissions from European soils under different land use: effects
679 of soil moisture and temperature, *European Journal of Soil Science*, 61, 683-696, 10.1111/j.1365-
680 2389.2010.01277.x, 2010.

681 Schindelin, J., Arganda-Carreras, I., Frise, E., Kaynig, V., Longair, M., Pietzsch, T., Preibisch,
682 S., Rueden, C., Saalfeld, S., and Schmid, B.: Fiji: an open-source platform for biological-image
683 analysis, *Nature methods*, 9, 676-682, 2012.

684 Schlüter, S., Sheppard, A., Brown, K., and Wildenschild, D.: Image processing of multiphase
685 images obtained via X-ray microtomography: A review, *Water Resources Research*, 50, 3615-
686 3639, 2014.

687 Schlüter, S., Henjes, S., Zawallich, J., Bergaust, L., Horn, M., Ippisch, O., Vogel, H.-J., and
688 Dörsch, P.: Denitrification in Soil Aggregate Analogues-Effect of Aggregate Size and Oxygen
689 Diffusion, *Frontiers in Environmental Science*, 6, 10.3389/fenvs.2018.00017, 2018.

690 Schurgers, G., Dorsch, P., Bakken, L., Leffelaar, P., and Haugen, L. E.: Modelling soil
691 anaerobiosis from water retention characteristics and soil respiration, *Soil Biology &
692 Biochemistry*, 38, 2637-2644, 10.1016/j.soilbio.2006.04.016, 2006.

693 Sexstone, A. J., Revsbech, N. P., Parkin, T. B., and Tiedje, J. M.: Direct measurement of oxygen
694 profiles and denitrification rates in soil aggregates, *Soil science society of America journal*, 49,
695 645-651, 1985.

696 Sierra, J., and Renault, P.: Respiratory Activity and Oxygen Distribution in Natural Aggregates in
697 Relation to Anaerobiosis, *Soil Science Society of America Journal*, 60, 1428-1438,
698 10.2136/sssaj1996.03615995006000050020x, 1996.

699 Sistrom, W. R.: A Requirement for Sodium in the Growth of *Rhodopseudomonas spheroides*,
700 *Microbiology*, 22, 778-785, 1960.

701 Smith, K. A.: A model of the extent of anaerobic zones in aggregated soils, and its potential
702 application to estimates of denitrification, *Journal of Soil Science*, 31, 263-277, 10.1111/j.1365-
703 2389.1980.tb02080.x, 1980.

704 Smith, K. A., Ball, T., Conen, F., Dobbie, K. E., Massheder, J., and Rey, A.: Exchange of
705 greenhouse gases between soil and atmosphere: interactions of soil physical factors and
706 biological processes, *European Journal of Soil Science*, 54, 779-791, 10.1046/j.1351-
707 0754.2003.0567.x, 2003.

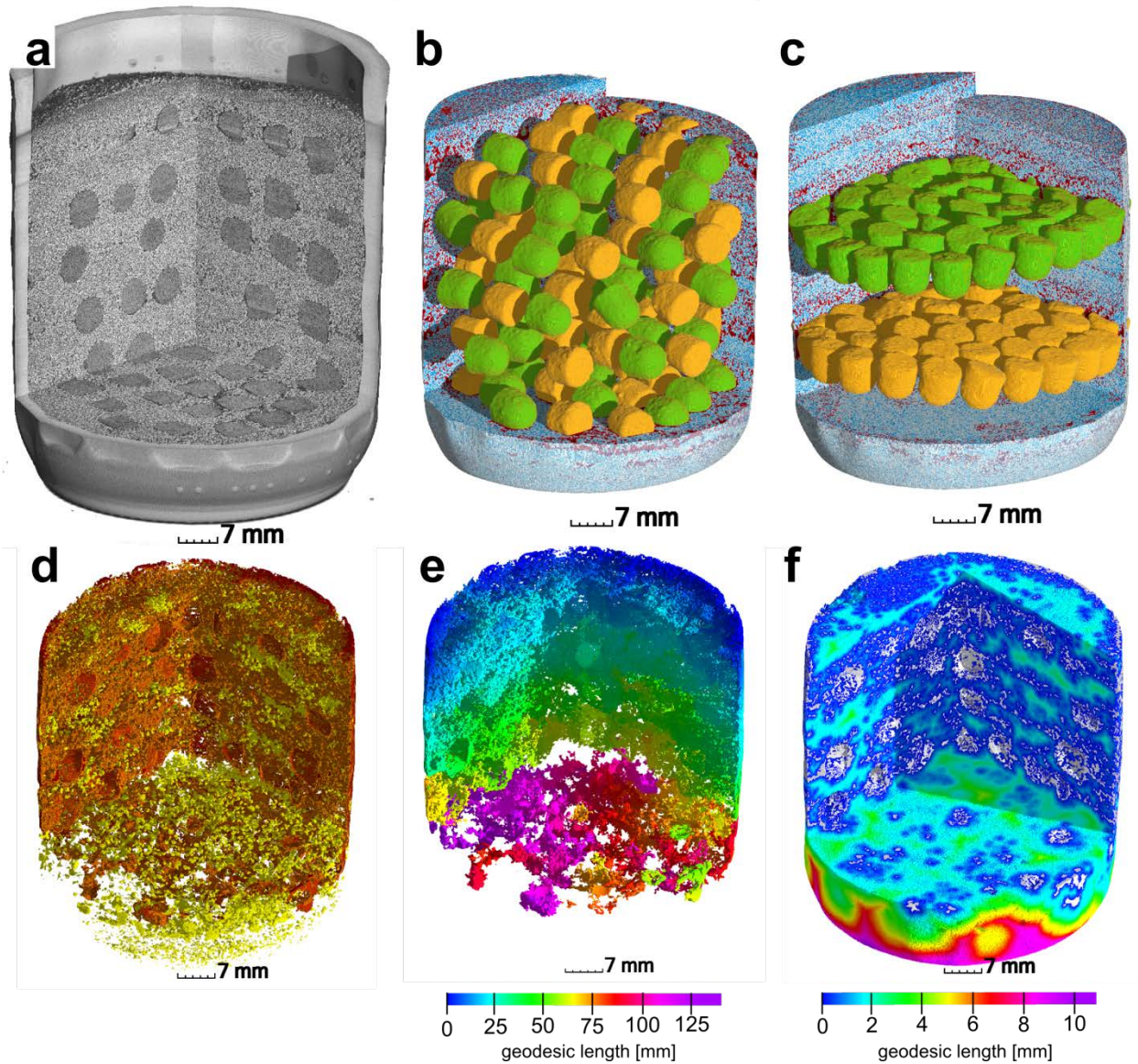
708 Tecon, R., and Or, D.: Biophysical processes supporting the diversity of microbial life in soil,
709 *FEMS Microbiology Reviews*, 41, 599-623, 10.1093/femsre/fux039, 2017.

710 Wang, B., Brewer, P. E., Shugart, H. H., Lerdau, M. T., and Allison, S. D.: Soil aggregates as
711 biogeochemical reactors and implications for soil-atmosphere exchange of greenhouse gases—A
712 concept, *Global Change Biology*, 0, doi:10.1111/gcb.14515, 2019.

713 Wanzek, T., Keiluweit, M., Varga, T., Lindsley, A., Nico, P. S., Fendorf, S., and Kleber, M.: The
714 Ability of Soil Pore Network Metrics to Predict Redox Dynamics is Scale Dependent, *Soil
715 Systems*, 2, 66, 2018.

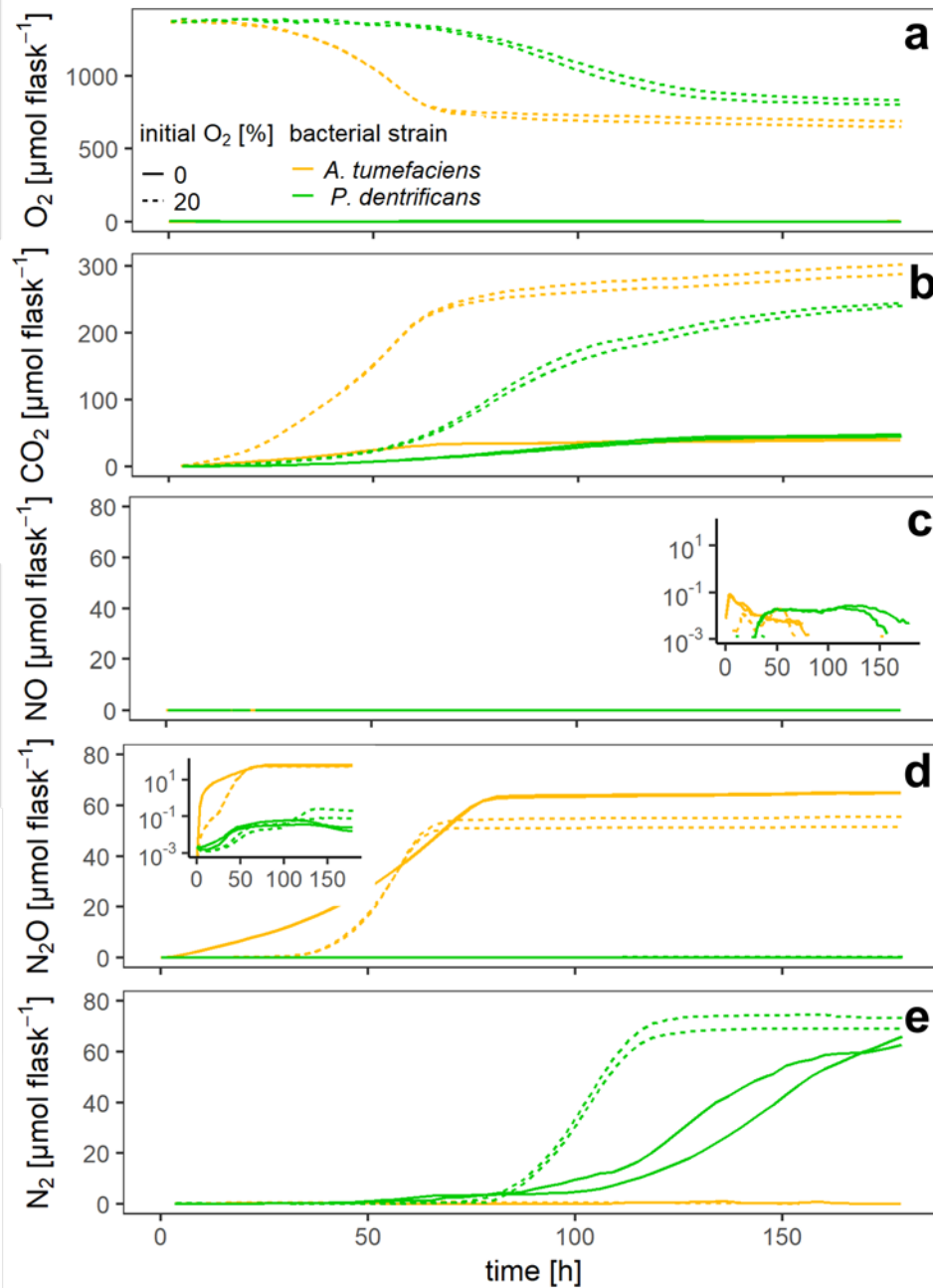
716 Weier, K. L., Doran, J. W., Power, J. F., and Walters, D. T.: Denitrification and the
717 Dinitrogen/Nitrous Oxide Ratio as Affected by Soil Water, Available Carbon, and Nitrate, *Soil
718 Science Society of America Journal*, 57, 66-72, 10.2136/sssaj1993.03615995005700010013x,
719 1993.

720 Zausig, J., Stepniewski, W., and Horn, R.: Oxygen Concentration and Redox Potential Gradients
721 in Unsaturated Model Soil Aggregates, *Soil Science Society of America Journal*, 57, 908-916,
722 10.2136/sssaj1993.03615995005700040005x, 1993.



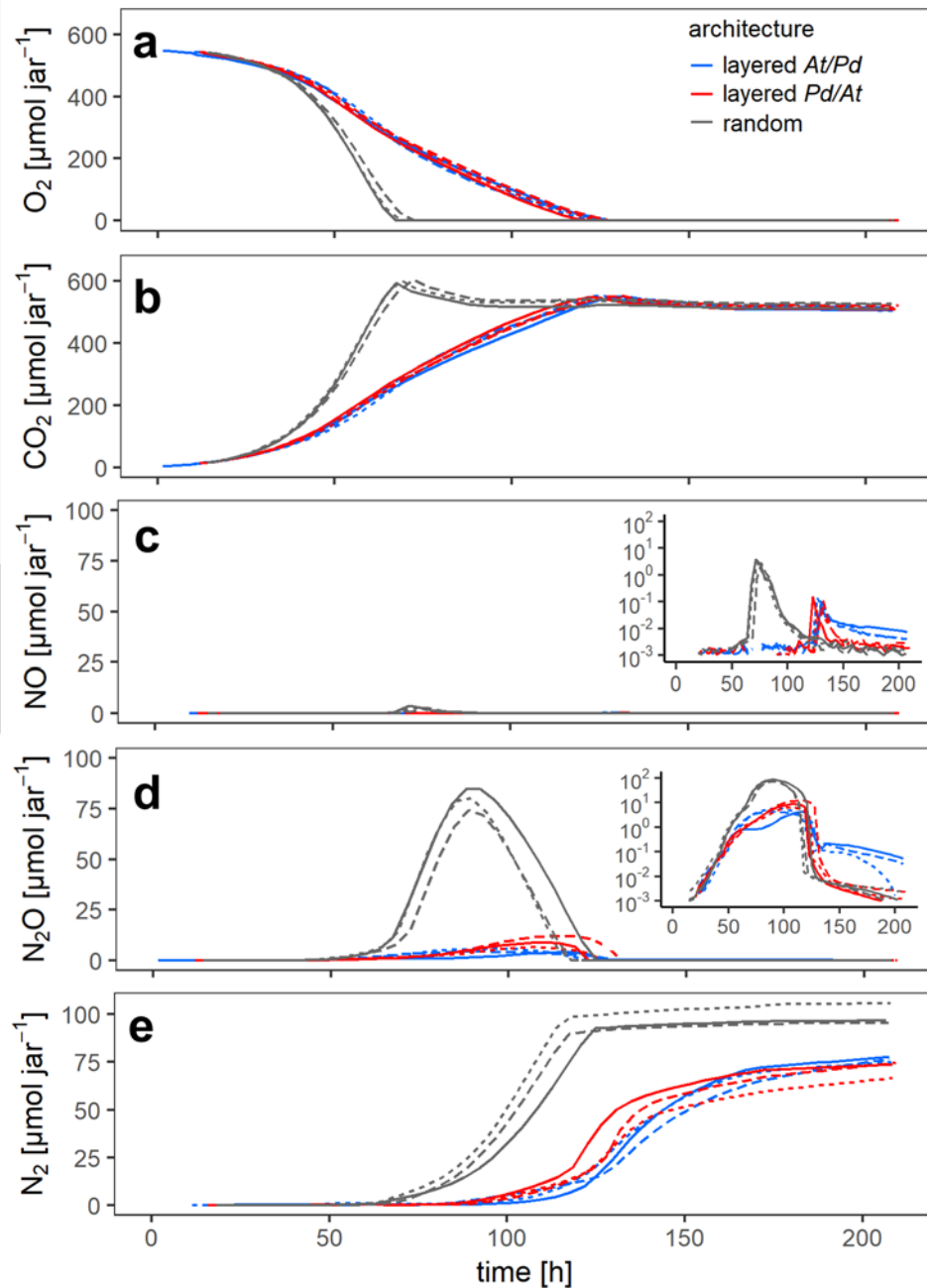
724

725 Figure 1. Upper panel: (a) X-ray CT scan of an incubation jar with random hotspot architecture and medium saturation
 726 (60% WFPS). (b) Image segmentation of the same jar into air (red), water (blue), sand (transparent), *A. tumefaciens*
 727 hotspots (orange) and *P. denitrificans* hotspots (green). (c) A different jar at medium saturation (60% WFPS) with layered
 728 *Pd/At* hotspot architecture. Lower panel: a jar with random distribution at high saturation (90% WFPS). (d) Air
 729 connectivity, determined as the volume fraction of air connected to the headspace (red, disconnected air shown in yellow).
 730 (e) Air tortuosity as derived from the geodesic length to the headspace within the connected air cluster. (f) Diffusion
 731 lengths determined as the geodesic length to the closest connected air cluster (white) within water-filled pores.



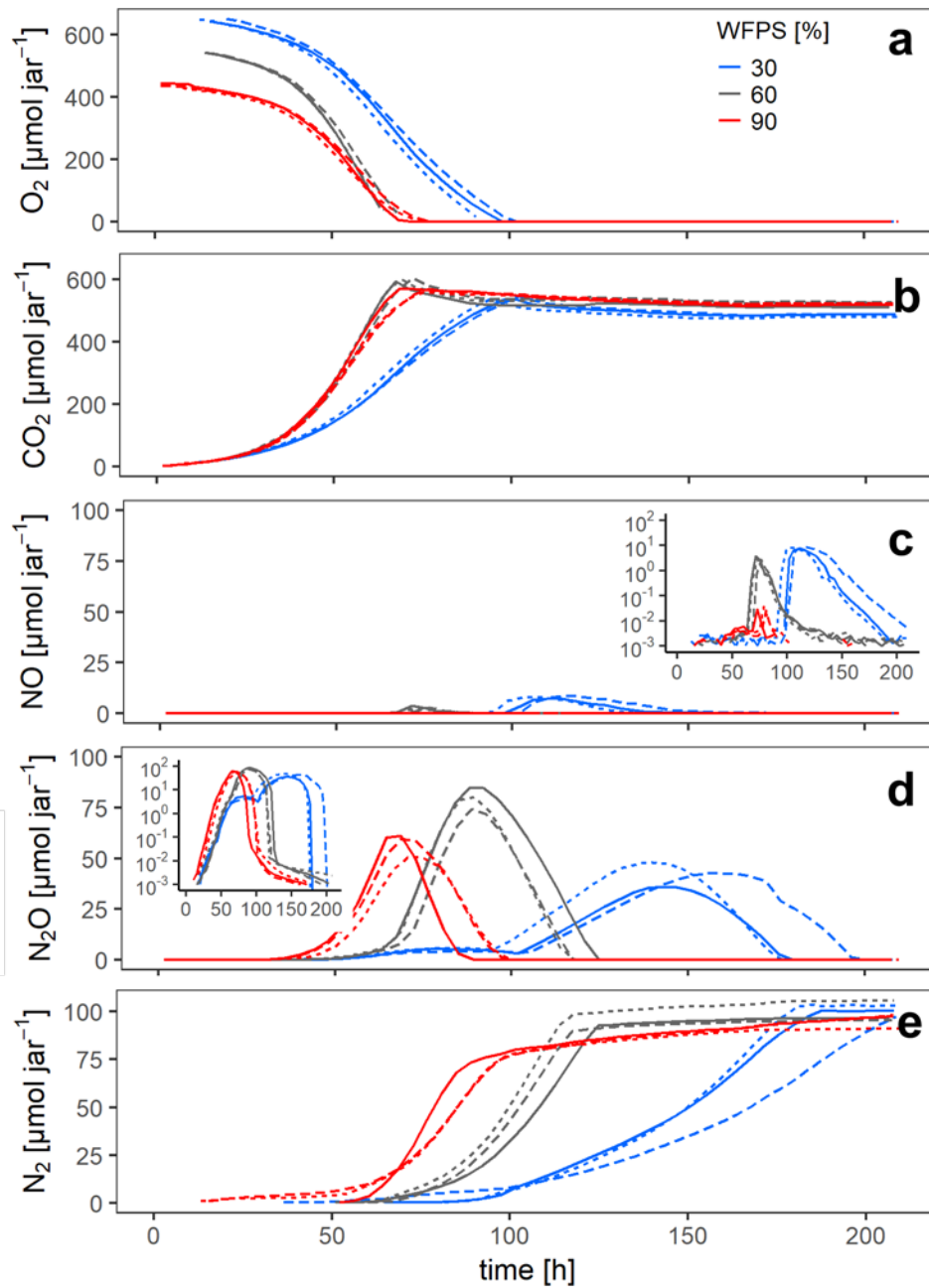
732

733 Figure 2: Gas kinetics of individual sets of hotspots that were loosely placed in empty flasks (fifty each), saturated with a
 734 growth medium and inoculated with two different bacterial strains – either a full denitrifier (*P. denitrificans*) or a
 735 truncated denitrifier lacking N2O reductase (*A. tumefaciens*), under oxic and anoxic conditions: (a) O₂, (b) CO₂, (c) NO,
 736 (d) N₂O, (e) N₂. **Note the logarithmic ordinate in (c) and (d).**



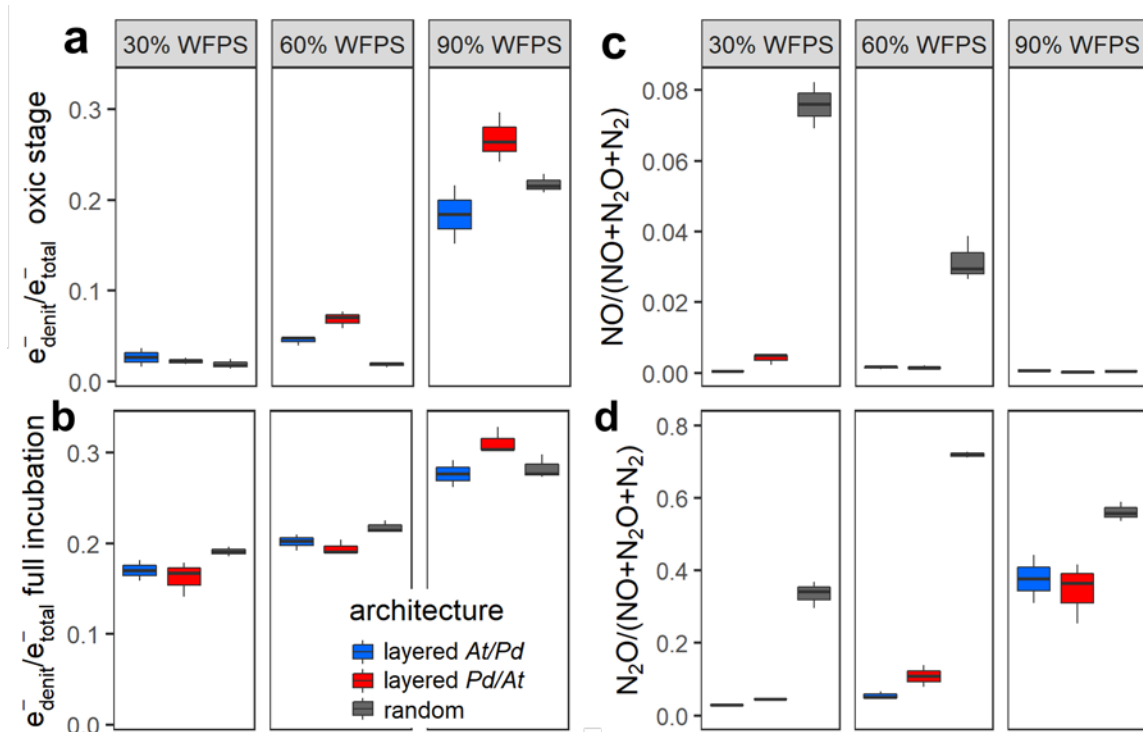
737

738 Figure 3: Gas kinetics in all treatments at medium saturation in the sand (60% WFPS) and an initial O₂ concentration of
 739 20% in the headspace for three different hotspot architectures containing a total of 100 hotspots, in which the hotspots
 740 either had maximum separation distance (random) or were densely packed in layers either with all At hotspots (layered
 741 At/Pd) or all Pd hotspots (layered Pd/At) in the upper layer : (a) O₂, (b) CO₂, (c) NO, (d) N₂O, (e) N₂. Note the logarithmic
 742 ordinate in (c) and (d). Data is only shown for the first 210h of the incubation period (300h total). Different line styles
 743 represent replicates.



744

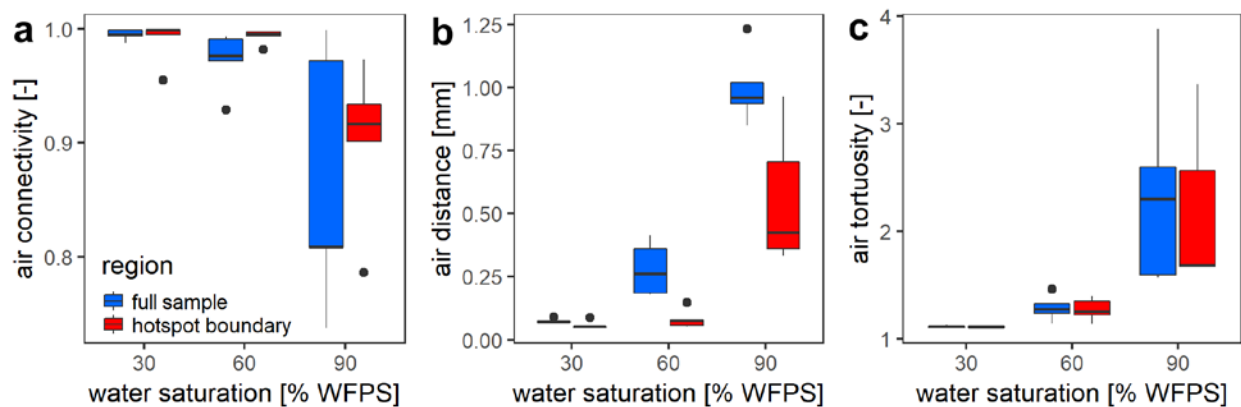
745 Figure 4: Gas kinetics of randomly placed hotspots at three different saturations in the sand and an initial O₂
 746 concentration of 20% in the headspace; (a) O₂, (b) CO₂, (c) NO, (d) N₂O, (e) N₂. Note the logarithmic ordinate in (c) and
 747 (d). Different lines styles represent replicates.



748

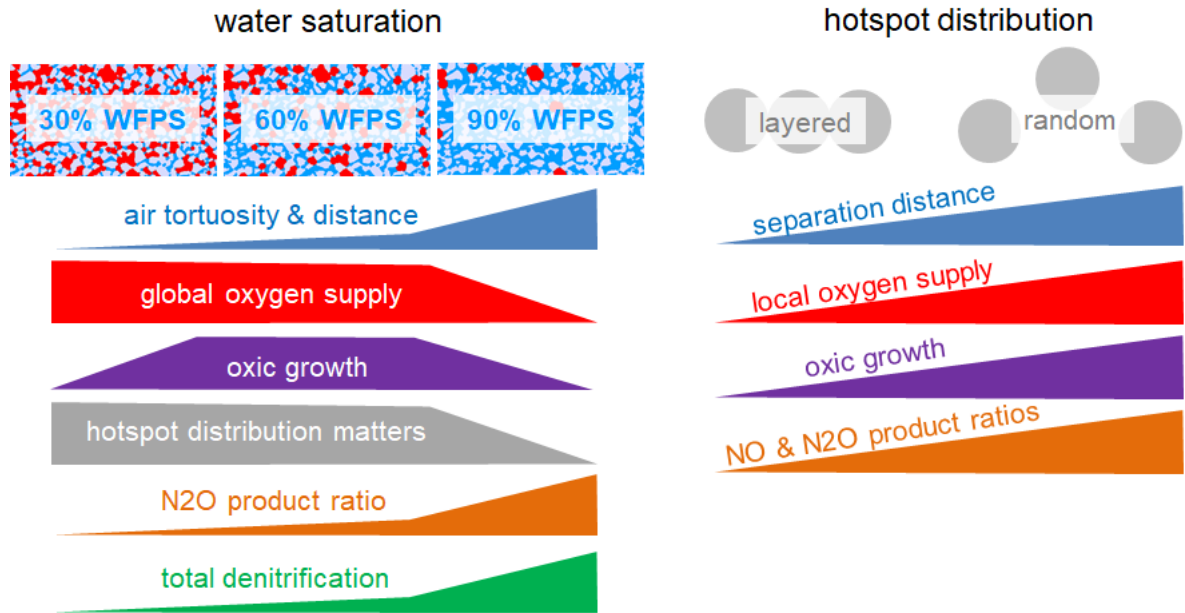
749 Figure 5: The proportion of denitrification in total respiration expressed as relative electron flow for all architectures and
 750 saturations. Values are reported for (a) the initial, oxidic to hypoxic stage (O_2 present in headspace) and (b) for the full
 751 incubation period of 300 h. The product ratios for NO (c) and N_2O (d) consider the full incubation period and are
 752 corrected for the release of precursor gases. Data shown as box-whisker plots: Whiskers- min-max, middle lines - median.

753



754

755 Figure 6: Morphological properties of air-filled pores at different saturations averaged over different hotspots
 756 architectures ($n=5$). These properties are reported separately for the entire pore space within the region of interest (full
 757 sample) and for the pore space in direct vicinity to the porous glass beads (hotspot boundary): (a) air connectivity
 758 represents the volume fraction of air with direct connection to the headspace. (b) Air tortuosity represents the ratio
 759 between geodesic length to the headspace and Euclidean distance for any voxel within the connected air-cluster. (c) Air
 760 distance represents the geodesic distance to the connected air cluster within the water-filled pores. Data shown as box-
 761 whisker plots: Whiskers- min-max, middle lines – median, dots: outliers.



762

763

764

765

Figure 7: Summary of the experimental findings about the impact of water saturation and spatial hotspot distribution on the physical constraints on the supply of hotspots with oxygen, the resulting growth rates and the implication of various aspects of denitrification.